

Hybrid Analog-Digital Simulation of the Abelian Higgs model

Muhammad Asaduzzaman,^{1,2,*} Rayleigh W. Parker,^{3,4,*} Noah Goss,^{5,6} Ahmed I. Mohamed,^{3,4} Max Neiderbach,^{3,7} Zane Ozzello,² Ravi K. Naik,⁶ Alexander F. Kemper,¹ Irfan Siddiqi,^{5,6} Yannick Meurice,² and Machiel S. Blok^{3,4}

¹*Department of Physics and Astronomy, North Carolina State University, Raleigh, NC 27607, USA*

²*Department of Physics and Astronomy, The University of Iowa, Iowa City, IA 52242, USA*

³*Department of Physics and Astronomy, University of Rochester, Rochester, New York 14627, USA*

⁴*University of Rochester Center for Coherence and Quantum Science, Rochester, New York 14627, USA*

⁵*Department of Physics, University of California, Berkeley, Berkeley, CA 94720, USA.*

⁶*Computational Research Division, Lawrence Berkeley National Laboratory, Berkeley, CA 94720, USA.*

⁷*Department of Physics, University of Maryland,*

4150 Campus Dr, College Park, MD 20742, USA

(Dated: March 16, 2026)

To investigate gauge theories with near-term quantum computers warrants exploration of non-traditional quantum simulators to find resource-efficient simulation protocols and ultimately access exotic features of different field theories, including unexplored regimes of the QCD phase diagram. In this work, using superconducting transmon qutrit processors, we formulate and implement a pulse-based, three-level, hybrid analog-digital simulation protocol of the (1+1) dimensional Abelian Higgs model (AHM) on two sites. Alongside this approach, we experimentally realize a gate-based implementation of the same model. Using the natural mapping of the three-level truncation of the transmon Hilbert space to the spin-1 truncated AHM, we observe real time dynamics of AHM field observables, which are analogous to electric field operators, with both protocols. For the analog-digital protocol, we engineer a Floquet simulation with a combination of local analog drives, driven modification of the natural interaction Hamiltonian of the two transmons, and dynamical decoupling pulses. For the digital protocol, we use a state-of-the-art qutrit processor to implement a Trotterized simulation of the model incorporating advanced error mitigation techniques. We further discuss the scalability of the two approaches, and their potential to be extended to the simulation of other model Hamiltonians. Our experiments demonstrate a viable platform for future studies of spin-1 and SU(3) based gauge theory models on current and near-term transmon qutrit processors.

I. INTRODUCTION

The prospect of simulating quantum field theories with quantum simulators has attracted considerable interest in recent years. While classical numerical methods based on importance sampling have successfully established lattice quantum chromodynamics (QCD) with imaginary time as a reliable nonperturbative formulation of strong interactions, they face significant challenges in addressing the *sign problem* that appears in the presence of large chemical potential [1, 2] and the difficulty of observing real-time non-equilibrium dynamics [3]. In light of these difficulties, there have been several efforts to simulate lattice gauge theories with various quantum computing platforms including superconducting circuits, trapped ions, and Rydberg atom simulators in (1+1) dimensions [4–9] and (2+1) dimensions [10–19]. These studies mark essential intermediate steps towards simulating QCD in (3+1) dimensions, and they address diverse physical phenomena including phase transitions [20], scattering of particles [9], real-time confining dynamics [7, 19], quench dynamics [21], the role of entanglement in thermalization [22], and quantum chaos [15].

So far, most studies have been performed on platforms composed of quantum two-level systems, or qubits. Plat-

forms made of *qudits*, or quantum d -level systems, however, have the potential to reduce the gate depths and non-local quantum operations required for quantum simulations of the naturally d -level systems that are common in lattice field theory models [23–26]. And yet, despite recent successes in the development of qudit processors with superconducting circuits [27, 28], trapped ions [29], and photonic systems [30], and despite a number of theoretical proposals to study field theories with qudits [26, 31–40], to our knowledge, there has been only a single experimental realization of a qudit-based field theory simulation, which was demonstrated on trapped-ion quantum hardware [18].

In this work, we consider a particular lattice field theory model—the spin-1 truncated Abelian Higgs model (AHM) [41–44] in two spacetime dimensions—and perform qudit-based quantum simulations of the model in superconducting circuit platforms with two separate but complementary approaches (Fig. 1). In the first, we leverage Hamiltonian engineering techniques to perform an analog-digital hybrid simulation, while in the second, we perform a fully digital simulation, taking advantage of state-of-the-art error mitigation methods. The AHM is a useful testbed for proof-of-principle simulators, not least because of its shared features with QCD, including confinement [45, 46], and string breaking [42], making it a valuable step towards quantum simulation of QCD. Here we consider the model on two lattice sites, but the methods may be applied more generally

* These authors contributed equally to this work.

to longer chains. Owing to the spin-1 truncation of the model, each site can be naturally mapped to a qutrit ($d = 3$), which in both simulation methods we encode in a truncated subspace spanned by the lowest three energy eigenstates of a transmon. Transmons are superconducting anharmonic oscillators whose nonlinearity enables high fidelity universal control over a portion of their Hilbert space [47]. Although they were initially engineered to implement qubits, they are seeing increasing use in higher-dimensional quantum computation and simulation [27, 28, 48–51].

In our first simulation approach, we engineer the Hamiltonian of a two-transmon system to approximate that of the target model with a hybrid analog-digital protocol, producing an effective Floquet Hamiltonian by alternating between periods of analog evolution and relatively short sequences of digital gates [52–54]. Similar methods have been used for previous quantum simulations in a wide variety of platforms [55–61]. These experiments have demonstrated analog-digital hybrid methods to be a powerful tool for quantum simulation, as they enable the reduction or elimination of relatively low-fidelity two-qutrit gates, while retaining some of the flexibility provided by fine-tuned digital control.

In our second approach, we perform a digital gate-based simulation of our model on a pair of transmons in a universal qutrit processor [62, 63]. Compared to a qubit-based gate decomposition of the model, we observe a four-fold reduction in resource requirements when decomposing the desired entangling operation with qutrit-based quantum gates. We incorporate state-of-the-art error mitigation protocols including randomized compilation and purification methods to compute observables that in future studies could identify phase transitions in large lattices. Our investigation demonstrates that resource requirements for digital error mitigation with twirling do not increase significantly when qubits are replaced with qutrits as the computational unit, in agreement with previous studies [63].

This paper is structured as follows. In Sec. II, we review an experimentally accessible lattice Hamiltonian formulation of the Abelian Higgs model. In Sec. III, we introduce the analog simulation approach for a single-site AHM and an analog-digital hybrid approach for the multi-site AHM Hamiltonian. We discuss the practical considerations for designing and implementing this protocol and present the results obtained in experiment. Next, in Sec. IV we decompose the unitary operation generated by the AHM Hamiltonian into the native gate set of our processor. We present the results obtained from the device and discuss the implications of different error mitigation strategies in our digital quantum simulation. Finally, we discuss the trade-offs and scalability of the two approaches in Sec. V and present our conclusions in Sec. VI.

II. ABELIAN-HIGGS MODEL

The Abelian Higgs model is a toy model of scalar quantum electrodynamics that describes the interaction of a photon field with spin zero particles. We begin with a brief description of the model and its approximate representation as a spin-1 Hamiltonian on the lattice. The action for the model is described by a $U(1)$ gauge field and a complex matter field Φ [33, 64, 65]

$$S = \int d^2x \frac{1}{4} \mathcal{F}_{\mu\nu} \mathcal{F}^{\mu\nu} + |D_\mu \Phi|^2 + \frac{\mu^2}{2} \Phi^\dagger \Phi - \frac{\lambda}{4} (\Phi^\dagger \Phi)^2, \quad (1)$$

where $\mathcal{F}_{\mu\nu} = \partial_\mu A_\nu - \partial_\nu A_\mu$ is the electromagnetic tensor and $D_\mu = \partial_\mu + iqA_\mu$ is the covariant derivative with matter charge q . The model is invariant under the $U(1)$ gauge transformation $\Phi \rightarrow e^{i\alpha(x)}\Phi$, $A_\mu \rightarrow A_\mu - \frac{1}{q}\partial_\mu\alpha(x)$. We work in the limit where the Higgs mode is decoupled and the complex scalar field is reduced to a constant multiplied by a complex phase (the Nambu-Goldstone mode). In (1+1) dimensions, this model has no deconfining phase; in higher dimensions, however, it does exhibit a similar confining feature of a charge and anti-charge pair [42, 43]. Confinement is marked by a linear growth in potential due to static charge separation below a critical distance scale and string breaking phenomena is observed at large distances signifying charge screening [66]. In real-time quantum simulators, both the confining feature and string breaking phenomena can be observed from the local charge density [67]. The shape of the light cone can identify confining features in the model and string breaking can be identified from the integrated local charge density by counting the number of charges present.

The action is translated into a discretized form by placing the matter fields on the vertices and gauge fields on the links of a 2D lattice—as illustrated in Fig. 1(a)—which can also be used for classical numerical simulation of the model using the path integral formulation. Taking the time continuum limit of the lattice action following the steps outlined in Ref. [5], we obtain the lattice Hamiltonian on N_s sites, assuming open boundary conditions,

$$H_{\text{AHM}} = \frac{\kappa}{2} \sum_{k=1}^{N_s} \left(L_z^{(k)} \right)^2 - \chi \sum_{k=1}^{N_s} F_x^{(k)} + \frac{\beta}{2} \sum_{k=1}^{N_s-1} \left(L_z^{(k+1)} - L_z^{(k)} \right)^2. \quad (2)$$

We define $\hbar = 1$ throughout this work. The L_z operator appearing in the Hamiltonian formulation is the canonical conjugate of the gauge field and is analogous to electric field operator in quantum electrodynamics, whereas charge corresponds to the conjugate of the phase operator of the Higgs field. In this (1+1) dimensional model, we do not need to account for the matter fields explicitly, as the charge can be computed as the difference of the

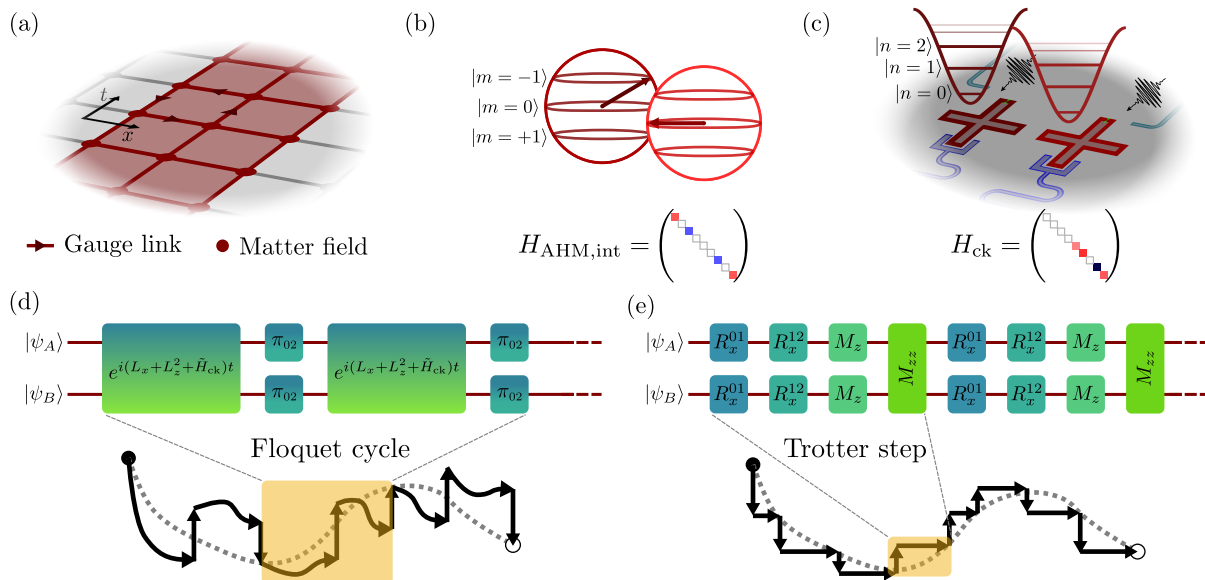


FIG. 1: (a) Lattice field theory representation of the Abelian Higgs model (AHM) in (1+1) dimensions. Vertices represent matter fields and edges represent gauge links in the discretized spacetime. In this work we consider a time-slice that is two plaquettes wide. (b) In the appropriate limits and approximations (see Ref. [5]), the (1+1)D AHM can be mapped to a spin-1 chain, where the spin states correspond to the plaquette quantum numbers. We illustrate the two spin-1 particles we simulate in this experiment along with the shape of their interaction Hamiltonian $H_{\text{AHM,int}} \propto L_z \otimes L_z$. (c) Our experimental platform consists of a pair of transmon qutrits, whose native cross-Kerr interaction H_{ck} is diagonal but differs greatly in form from the target interaction. By applying microwave drives to the two transmons, we may approximate evolution under the model Hamiltonian in two distinct ways. (d) An analog-digital hybrid approach to engineering the evolution of the target Hamiltonian. Here we alternate between evolution under a Hamiltonian engineered with analog drives and approximately instantaneous local π_{02} gates, which transpose the states $|0\rangle$ and $|2\rangle$ on each transmon individually. (e) The fully digital approach. Here a sequence of digital gates drawn from a universal set is repeated to effectively Trotterize the time evolution. Definitions of the gates are given in Sec. IV. For both protocols, a sketch of the trajectory of the state is shown. In the analog-digital simulation, the evolution can deviate substantially from the ideal trajectory (dashed line) but returns after a full Floquet cycle up to the error in the Magnus expansion. In the digital simulation, the evolution is closer to the exact solution throughout the evolution, and approximates it up to Trotter error at the end of each Trotter step.

electric field operators $(L_z^{k+1} - L_z^k)$, due to Gauss's Law. The terms in the Hamiltonian can be interpreted as the local energy of the electric field; an injection of energy that drives local evolution of the field; and the cost in energy due to creation of charges, respectively. The operators $L_z^{(k)}$, where k indexes the site that the operator acts on, are identical to the angular momentum operator defined by

$$L_z |m\rangle = m |m\rangle. \quad (3)$$

The operators $F_x^{(k)}$ are defined by the following equations:

$$F_{\pm} |m\rangle = |m \pm 1\rangle, \quad F_x = \frac{1}{2} (F_+ + F_-). \quad (4)$$

To capture the model exactly, the operators $L_z^{(k)}$ and $F_x^{(k)}$ are required to act on infinite levels: $m \in \{0, \pm 1, \pm 2, \dots, \pm \infty\}$, but in practice, some cutoff $|m| \leq l$ is required. In this work we take $l = 1$, and in this case we

may identify $\sqrt{2}F_x$ with the spin-1 L_x operator. We may map spin L_z eigenstates to transmon eigenstates with

$$\begin{aligned} |m = 1\rangle &\rightarrow |n = 0\rangle, & |m = 0\rangle &\rightarrow |n = 1\rangle, \\ |m = -1\rangle &\rightarrow |n = 2\rangle. \end{aligned} \quad (5)$$

This spin-1 truncation does not recover the continuum limit of the theory, but it allows for the development of new tools for simulating various gauge theory models with a more efficient encoding than is available on qubit platforms. In addition, the aspect of triality in a spin-1 model is intriguing for its connection to QCD, where physical states transform under the center of the gauge group $\text{SU}(3)$.

III. ANALOG-DIGITAL SIMULATION

We first discuss the analog-digital simulation of the Abelian Higgs model on two sites. Experiments in this section were performed on a Rochester-based transmon

device with properties given in Table I. The implementation can be broken into two parts: (1) driving single-transmon dynamics to emulate local on-site terms in the model, and (2) engineering the interaction between the transmons to effectively match the $L_z \otimes L_z$ interaction term between the sites in the model. To reduce Trotterization errors and to maximize simulation time, we aim to perform these operations simultaneously, which introduces an additional challenge: designing the drives for the single-site dynamics and the interaction-engineering in such a way that each does not interfere with the other's operation.

A. Single-qutrit implementation

We begin by discussing the analog drives that produce the desired single-transmon Hamiltonian at each site. In the frame of the lab, the Hamiltonian of transmon k truncated to three levels, with a time-dependent drive $V_k(t)$ may be written [47]

$$\begin{aligned} H_k^{\text{LF}}(t) &= H_k^0 + H_k^{\text{drive}}(t) \\ &= \omega_{01}^k |1\rangle\langle 1| + (\omega_{01}^k + \omega_{12}^k) |2\rangle\langle 2| \\ &\quad + V_k(t) (i |1\rangle\langle 0| + i\lambda_k |2\rangle\langle 1| + \text{h.c.}), \end{aligned} \quad (6)$$

where ω_{ij}^k is defined as the transition frequency between transmon eigenstates $|i\rangle$ and $|j\rangle$, and $\lambda_k \approx \sqrt{2}$ is a dimensionless factor which characterizes the ratio between the charge couplings to the $|1\rangle \leftrightarrow |2\rangle$ transition and the $|0\rangle \leftrightarrow |1\rangle$ transition. For the remainder of this subsection, we will suppress the transmon index k on terms in the Hamiltonian.

We drive both transitions simultaneously, taking $V(t) = \sum_{i=1}^2 \Omega_i(t) \cos(\omega_i^{\text{d}} t + \phi_i)$ where Ω_i are the drive envelopes, ω_i^{d} are the drive frequencies, and ϕ_i are the phases on each drive term. We further define detunings $\Delta_i = \omega_i^{\text{d}} - \omega_{i-1,i}$ and assume $|\Delta_i| + \Omega_i \ll |\omega_{12} - \omega_{01}|$, so that each drive term is close to resonance with only one transition. For both transmons in the analog-digital experiment, the anharmonicity was roughly $(\omega_{12} - \omega_{01})/2\pi \sim -240$ MHz.

Extracting the on-site terms from the model Hamiltonian in Eq. (2), we find

$$H_{\text{AHM},k} = \frac{\kappa + \beta}{2} L_z^2 - \frac{\chi}{\sqrt{2}} L_x, \quad (7)$$

where site k is taken to be at the boundary of the chain for both sites of the two-site model. To find the drives required to simulate $H_{\text{AHM},k}$, we first perform a unitary rotating frame transformation to take H_k^{LF} into the frame of the drive frequencies: $H_k^{\text{DF}} = U_{\text{D}}^\dagger H_k^{\text{LF}} U_{\text{D}} - i U_{\text{D}}^\dagger \partial_t U_{\text{D}}$, where $U_{\text{D}}(t) = \text{diag}(1, e^{-i\omega_1^{\text{d}} t}, e^{-i(\omega_1^{\text{d}} + \omega_2^{\text{d}}) t})$ [68, 69]. Since this frame transformation is diagonal, the population dynamics we observe in the lab frame will be identical to the population dynamics in the rotating frame.

After applying the rotating wave approximation (RWA) under the assumptions that the drive strengths are weak compared to the drive frequencies and compared to the anharmonicity of the transmon, $\Omega_1, \Omega_2 \ll |\omega_{01} - \omega_{12}| < \omega_1^{\text{d}}, \omega_2^{\text{d}}$, we obtain,

$$\begin{aligned} H_k^{\text{DF}}(t) &\approx -\Delta_1 |1\rangle\langle 1| - (\Delta_1 + \Delta_2) |2\rangle\langle 2| \\ &\quad + \frac{i}{2} \Omega_1(t) e^{-i\phi_1} |1\rangle\langle 0| + \frac{i\lambda}{2} \Omega_2(t) e^{-i\phi_2} |2\rangle\langle 1| + \text{h.c.} \end{aligned} \quad (8)$$

More details of the terms dropped under the RWA can be found in Appendix B.

It is possible to map Eq. (8) to Eq. (7) by assuming equal drive phases $\phi_1 = \phi_2 = -\pi/2$, constant drive envelopes $\Omega_1(t) = \lambda\Omega_2(t) = \Omega_0$, and detunings $\Delta_1 = -\Delta_2 = \Delta_0$, which simplifies the driven transmon Hamiltonian to,

$$\begin{aligned} H_k^{\text{DF}} &\approx -\Delta_0 |1\rangle\langle 1| \\ &\quad - \frac{1}{2} \Omega_0 (|1\rangle\langle 0| + |2\rangle\langle 1| + \text{h.c.}) \\ &\rightarrow \Delta_0 L_z^2 - \frac{\Omega_0}{\sqrt{2}} L_x, \end{aligned} \quad (9)$$

where in the last step we have removed a global energy offset $-\Delta_0 I$. To convert between the dimensionless parameters in Eq. (7) and the physical parameters of Eq. (9), we must choose a time scale t_s , which sets a scale frequency t_s^{-1} . Then the mapping is complete with $\Omega_0 = \chi t_s^{-1}$ and $\Delta_0 = \frac{\kappa + \beta}{2} t_s^{-1}$. We have freedom in the single-qutrit experiment to choose the scale frequency as long as the RWA conditions are met. In the experiment shown in Fig. 2, we chose $t_s^{-1} = 1$ MHz.

While the above derivation assumed constant drive envelopes in the final step, the experiment must be performed with a shaped envelope, either explicitly or implicitly. To do so in a controlled manner, we give both drives the same envelope: $\Omega_1(t) = \lambda\Omega_2(t) = \Omega_0 A_T(t)$, where $A_T(t)$ is normalized such that its integral after a pulse of duration T is equal to the area of a unit step of the same duration: $\int_0^T A_T(t) dt = T$. The envelope function and its normalization are given explicitly in Appendix B. The unitary evolution produced at the end of the drive can be modeled with average Hamiltonian theory [70] (see also Appendix A), where, to first order, the average Hamiltonian is provided by independent time-averages of the individual matrix elements to produce the same result as in Eq. (9).

Second-order and higher terms in the average Hamiltonian produce coherent errors in the simulation. Because they depend on the commutator of the Hamiltonian with itself at different times, we chirp the pulses during the ramps to maintain instantaneous detunings with the same envelope as the drives, that is, $\Delta_{01}(t) = -\Delta_{12}(t) = \Delta_0 A_T(t)$. Details of the phase ramping necessary to maintain this relationship and the accompanying frame transformation can be found in Appendix B. The

single qutrit Hamiltonian may then be written,

$$\begin{aligned} H_k^{\text{DF}}(t) &\approx \Delta(t)L_z^2 - \frac{\Omega(t)}{\sqrt{2}}L_x \\ &\approx A_T(t) \left(\Delta_0 L_z^2 - \frac{\Omega_0}{\sqrt{2}}L_x \right), \end{aligned} \quad (10)$$

and the Magnus expansion then terminates after the first-order term.

As is illustrated in Fig. 2(a), to simulate evolution to different times, the pulse duration T is varied, and the drive envelope is stretched with a fixed amplitude and a ramp that is a fixed fraction $r = 0.1$ of the pulse duration. Then, regardless of T , the average Hamiltonian at the end of the pulse is

$$\bar{H}_k^{\text{DF}} \approx \Delta_0 L_z^2 - \frac{\Omega_0}{\sqrt{2}}L_x, \quad (11)$$

where the approximation is due only to the RWA.

The results of a single-transmon analog simulation experiment may be seen in Fig. 2(b), where we plot expectation values of the diagonal field operators L_z and L_z^2 , which are computed directly from measured transmon eigenstate populations, after a statistical readout correction has been applied [71, 72]. For this measurement, the parameters of Eq. (7) were set to $\kappa/2\pi = \chi/2\pi = 1$, $\beta = 0$. The exact single-qutrit dynamics predicted by the model are plotted along with the data, as well as a Lindblad master equation model described in Appendix E that takes into account independently measured decoherence and relaxation times for this transmon, as listed in Table I (Qutrit B). We see good agreement with the prediction of the Lindblad model, indicating that the errors in our single-transmon simulation are dominated by decoherence.

B. Two-qutrit implementation

1. Engineering the interaction Hamiltonian

We next discuss the analog-digital method for engineering the target interaction. The interaction part of the Hamiltonian in Eq. (2) takes the form of an Ising-type interaction,

$$H_{\text{AHM,int}} = -\beta L_z \otimes L_z. \quad (12)$$

Because we are performing the simulation on two sites only, we will indicate which site an operator acts on by where it falls relative to the \otimes symbol rather than a superscript index. In addition, when the meaning is clear from context, we will omit the \otimes symbol between operators acting on transmons A and B .

Our device consists of a pair of transmons that have a direct capacitive coupling, with properties given in Table I. Because our transmon qutrits are far detuned from

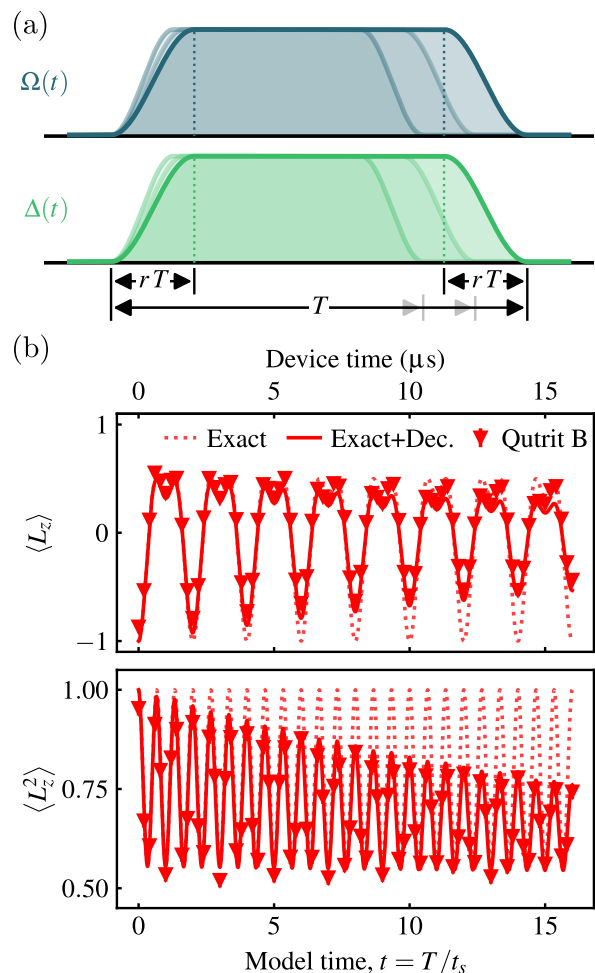


FIG. 2: Single qutrit analog experiment. (a) Protocol for performing a single-qutrit analog simulation of the Abelian Higgs model. Drives on both transitions of the qutrit follow the same envelope $\Omega_{01}(t) = \lambda\Omega_{12}(t) = \Omega(t) = \Omega_0 A_T(t)$ and have equal and opposite detunings $\Delta_1(t) = -\Delta_2(t) = \Delta(t) = \Delta_0 A_T(t)$. Each data point in (b) is measured by setting a pulse duration T and reading out qutrit eigenstate populations at the end of the pulse. The ramps are a fixed fraction $r = 0.1$ of the total duration, producing a stretching of the pulse for increasing T . The dimensionless envelope function $A_T(t)$ is normalized to have an area equal to its duration T ; see Appendix B for details. (b) Expectation values of field operators L_z (top) and L_z^2 (bottom) for a single qutrit under analog evolution starting in initial transmon state $|n = 2\rangle$, with $\kappa/2\pi = \chi/2\pi = 1$, $\beta = 0$. The scale frequency was chosen to be $t_s^{-1} = 1$ MHz and converts between physical device time (upper axis) and dimensionless model time (lower axis). Dotted lines show exact Schrödinger equation evolution under the model Hamiltonian, solid lines are master equation simulations assuming the independently measured dephasing and relaxation times of Qutrit B in Table I. Uncertainties are estimated from shot noise $\sigma \sim 1/\sqrt{N_{\text{shots}}}$ where $N_{\text{shots}} = 3000$.

each other relative to the strength of their capacitive coupling, their native interaction is effectively described by a dispersive *cross-Kerr* Hamiltonian [73, 74], which is described in more detail in Appendix C. We parameterize this diagonal interaction into a combination of powers of the L_z operators of the two qutrits,

$$H_{\text{ck}} = \sum_{i,j=0}^2 z_{ij} L_z^i \otimes L_z^j, \quad (13)$$

where $L_z^0 = I$ is the identity matrix. Terms that include L_z to a nonzero power on only one qutrit correspond to local frequency shifts, and may be removed by applying the proper frame rotations to each transmon individually. In the experiment, this corresponds to calibrating the frequencies of each qutrit when the other is in the $|1\rangle$ state, rather than the more common choice of tuning when the other is in the $|0\rangle$ state. This yields a simplified interaction Hamiltonian,

$$\begin{aligned} H'_{\text{ck}} &= \sum_{i,j=1}^2 z_{ij} L_z^i \otimes L_z^j \\ &= z_{11} L_z L_z + z_{12} L_z L_z^2 \\ &\quad + z_{21} L_z^2 L_z + z_{22} L_z^2 L_z^2. \end{aligned} \quad (14)$$

We then desire a method that can achieve effective interaction rates $z_{21} = z_{12} = z_{22} = 0$.

The values of z_{ij} measured for the transmon pair used in this experiment are shown in Fig. 3(a). They are sensitive to the spectra and charge matrix elements of the two transmons, (see Appendix C for calculations of the rates from second-order perturbation theory), and as a consequence, they cannot be expected in general to realize a native $L_z L_z$ interaction. We measure the rates in the experiment with a double-echo sequence [75], referred to as JAZZ in superconducting qubit literature [76], which we have adapted for use with qutrits, (see Appendix D).

Undesired interactions may often be canceled using dynamical decoupling techniques [54, 59, 77]. However, previously reported pulse sequences on qutrits that can produce the desired interaction involve pulses that do not commute with our single-qutrit drives [27]. Instead, we design a protocol that integrates the single-qutrit drives with a Hamiltonian engineering method based on simultaneous Stark drives on the two transmons and a minimal set of dynamical decoupling pulses, adapted from Ref. [78]. We apply Stark drives to both transmons, $\Omega_{S,A}(t) \cos \omega_S t$ and $\Omega_{S,B}(t) \cos \omega_S t$, where the envelopes $\Omega_{S,k}$ and the frequency ω_S provide a degree of tunability to the interaction Hamiltonian. This is also the principle behind the controlled-Z gates used in the gate-based simulation in Sec. IV.

In practice, a single pair of Stark drives only affords enough tunability to set one term in the interaction Hamiltonian to zero. With this degree of freedom in mind, we search for sequences consisting only of pulses that leave the single-qutrit Hamiltonians invariant and

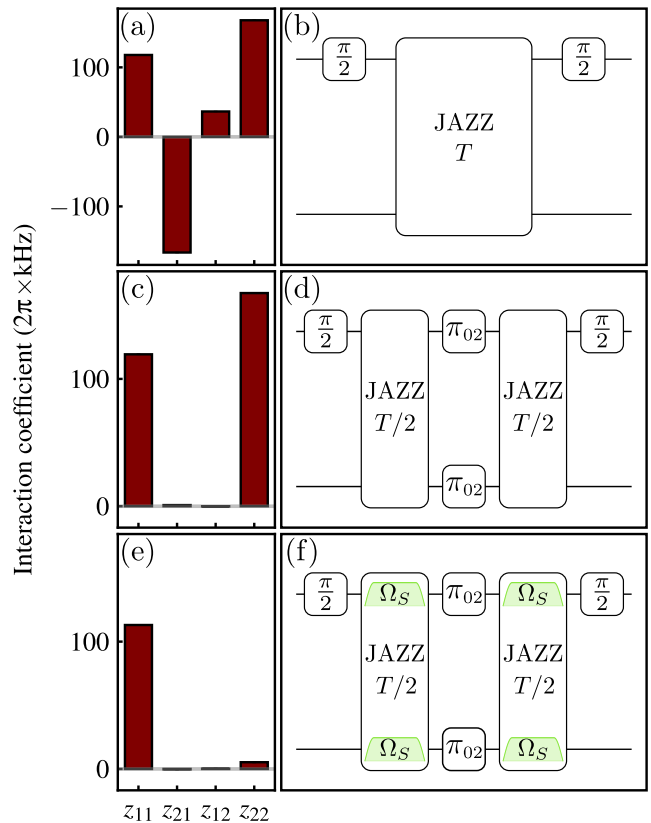


FIG. 3: Engineering the $L_z \otimes L_z$ interaction. (a) Experimentally measured interaction Hamiltonian terms from Eq. (13) for the undriven (bare) two-transmon system. (b) Abstract circuit schematic of the interaction rate measurement. The JAZZ block consists of two periods of free evolution of duration T , with a π pulse on both transmons between them [75, 76]. The subspaces of the π and $\pi/2$ pulses are determined by which matrix element of the interaction Hamiltonian is being targeted, as is explained in depth in Appendices C and D. (c)–(d) Interaction rates and measurement circuit schematic when averaging with a $|0\rangle \leftrightarrow |2\rangle$ swap. We observe that the rates for the odd-parity terms, z_{12} and z_{21} are effectively eliminated by this dynamical decoupling sequence, while the even-parity terms remain unchanged. The circuit now involves four periods of free evolution with duration $T/2$. (e)–(f) Interaction rates and circuit schematic with both averaging and Stark drives applied. Applying Stark drives at the appropriate frequency and amplitude nearly eliminates the driven \tilde{z}_{22} term, leaving the modified \tilde{z}_{11} as the only appreciable interaction rate in the Hamiltonian. See Appendix D for details on the calibration of the Stark drives.

that may lead to a cancellation of at least two of the undesired terms. Conveniently, the operation $U_{02} \equiv \pi_{02}^A \pi_{02}^B$, where π_{02}^k is a local unitary that transposes states $|0\rangle$ and $|2\rangle$ on transmon k , commutes with the single-transmon

average Hamiltonian in Eq. (11) and has the effect of flipping the signs on the odd-parity interaction terms while leaving the even-parity terms unchanged:

$$U_{02}H'_{\text{ck}}U_{02}^\dagger = z_{11}L_zL_z - z_{12}L_zL_z^2 - z_{21}L_z^2L_z + z_{22}L_z^2L_z^2. \quad (15)$$

By alternating periods of evolution under H_{ck} with dynamical decoupling pulses U_{02} , the system can be made to evolve under the dynamically-decoupled interaction Hamiltonian on average,

$$H_{\text{ck}}^{\text{dd}} = \frac{1}{2} \left(H'_{\text{ck}} + U_{02}^\dagger H'_{\text{ck}} U_{02} \right) = z_{11}L_zL_z + z_{22}L_z^2L_z^2. \quad (16)$$

As can be seen from average Hamiltonian theory (Appendix A), as long as the pulses that perform U_{02} are assumed to be instantaneous, this averaging is exact in the absence of other terms in the Hamiltonian, since H'_{ck} and $U_{02}H'_{\text{ck}}U_{02}^\dagger$ commute. The averaged interaction rates and the protocol for measuring them are shown in Figs. 3(c) and 3(d), respectively.

After this sequence, the only remaining undesired interaction term is $z_{22}L_z^2L_z^2$, and we find that for a proper choice of Stark drive frequency and amplitude, the coefficient $z_{22} \rightarrow \tilde{z}_{22}$ can be driven close to zero. This modifies all the coefficients in the driven interaction Hamiltonian, $z_{ij} \rightarrow \tilde{z}_{ij}$, and we refer to the new effective cross-Kerr interaction Hamiltonian as \tilde{H}'_{ck} and the effective driven and dynamically-decoupled interaction as $\tilde{H}_{\text{ck}}^{\text{dd}}$. The measured coefficients of $\tilde{H}_{\text{ck}}^{\text{dd}}$ are shown in Fig. 3(e). We observe that only the L_zL_z term has appreciable weight after applying the protocol. The calibration procedures for finding the Stark drive frequency and amplitudes required to achieve $\tilde{z}_{22} \approx 0$ are described in Appendices C and D, respectively.

While the single-qutrit experiment has great flexibility in the choice of scale frequency, in the two-qutrit experiment \tilde{z}_{11} is fixed after applying the Stark drives, and thus it sets the scale for the other terms in the Hamiltonian. That is, we have $\tilde{z}_{11} = -\beta t_s^{-1}$ with $\beta/2\pi \equiv 1$. The minus sign appears due to a mismatch in signs between $\tilde{z}_{11} > 0$ and the $-\beta L_zL_z$ term in the model Hamiltonian. We account for this by reversing the mappings of transmon states $|n=0\rangle$ and $|n=2\rangle$ in Eq. (5) for only one transmon, effectively conjugating its entire evolution with π_{02} , since $L_z \otimes \pi_{02}^\dagger L_z \pi_{02} = -L_z \otimes L_z$. This is done entirely in post-processing.

2. Combining on-site and interaction terms

We combine the single-qutrit drive Hamiltonians $H_k^{\text{DF}}(t)$ defined in Sec. III A with the Stark-driven interaction Hamiltonian by turning on all the drives simultaneously, as sketched for each pulse in Fig. 4(a), yielding

$$H_{\text{sys}}(t) = H_A^{\text{DF}}(t) + H_B^{\text{DF}}(t) + \tilde{H}'_{\text{ck}}(t), \quad (17)$$

for $t \in [0, T_E]$, where T_E is the fixed evolution period for a single pulse. To reduce errors caused by a failure of the Hamiltonian to commute with itself at different times throughout the pulse, we must ensure that the time dependence of $\tilde{H}'_{\text{ck}}(t)$, determined by the product $\Omega_{S,A}(t)\Omega_{S,B}(t)$, varies with the same envelope as the single-qutrit drives and detunings. Hence, we set the Stark drive envelopes to be $\Omega_{S,A}(t) = \Omega_{S,B}(t) = \Omega_S^0 \sqrt{A_{T_E}(t)}$. This does not entirely eliminate the error, as there remains the undriven component of the interaction Hamiltonian, which does not commute with the single-qutrit L_x terms. As we show in Appendix F, however, this error only enters to third order in the average Hamiltonian and scales roughly as $(rT_E)^2$, quadratically with the ramp duration.

We cannot reduce the ramp duration indefinitely, since we find in practice that the ramp must also be sufficiently long to maintain an adiabatic change of the interaction Hamiltonian. In this experiment, we chose a ramp duration of 80 ns. When the errors are made sufficiently small, the effective average Hamiltonian over the course of one pulse is well approximated by the first order term in the Magnus expansion,

$$\begin{aligned} \bar{H}_{\text{sys}} &\approx \frac{1}{T_E} \int_0^{T_E} H_{\text{sys}}(t) dt \\ &= \bar{H}_A^{\text{DF}} + \bar{H}_B^{\text{DF}} + \tilde{H}'_{\text{ck}}. \end{aligned} \quad (18)$$

Then alternating between periods of driven evolution and the π_{02} pulses—which in this experiment are performed by driving both $|0\rangle \leftrightarrow |1\rangle$ and $|1\rangle \leftrightarrow |2\rangle$ transitions simultaneously with zero detuning at a much larger amplitude than the on-site simulation drives [79, 80]—we arrive at the desired effective Floquet evolution:

$$\begin{aligned} U_{\text{eff}}(N) &= \left[\exp\left(-iU_{02}^\dagger \bar{H}_{\text{sys}} U_{02} T_E\right) \exp\left(-i\bar{H}_{\text{sys}} T_E\right) \right]^N \\ &\approx \exp\left(-i\left(\bar{H}_A^{\text{DF}} + \bar{H}_B^{\text{DF}} + \tilde{H}_{\text{ck}}^{\text{dd}}\right) N T_E\right), \end{aligned} \quad (19)$$

where \bar{H}_A^{DF} and \bar{H}_B^{DF} are given by Eq. (11) and $\tilde{H}_{\text{ck}}^{\text{dd}} \approx \tilde{z}_{11}L_zL_z$. This therefore approximates H_{AHM} .

The error in the approximation can be thought of in terms of both the higher-order terms in the Magnus expansion and Trotterization error. We analyze the error terms using AHT in Appendix F and find that they scale linearly in the evolution period T_E , suggesting that shorter evolution periods between the π_{02} gates will produce a better approximation. There is a tradeoff, however, with the requirement that the gates be effectively instantaneous. In practice, we find an acceptable balance with an evolution pulse duration $T_E = 800$ ns and a π_{02} gate time of $T_g = 60$ ns.

3. Device results

In Fig. 4(b) we plot dynamics from the experimental implementation of the analog-digital protocol, along

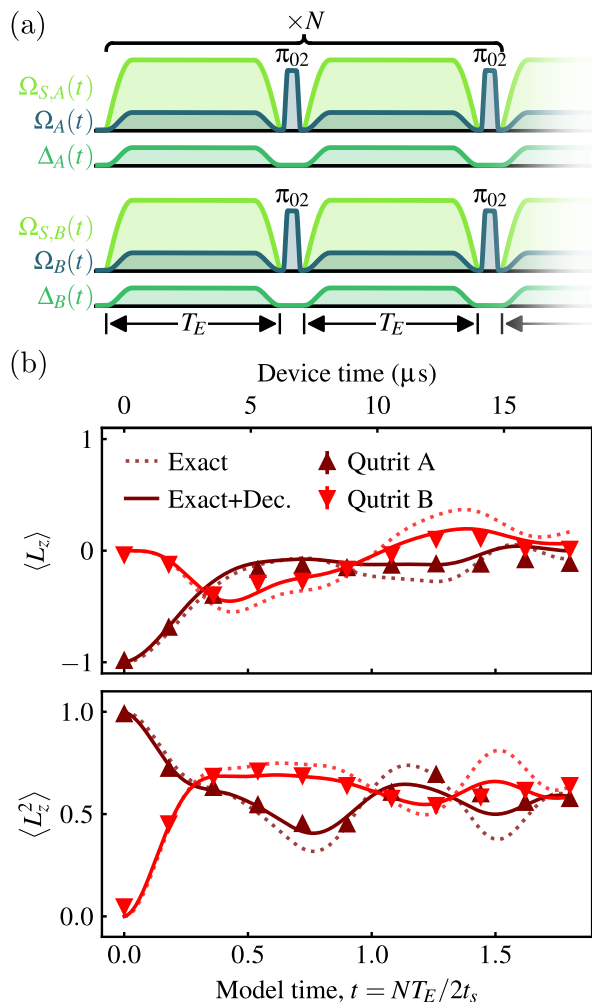


FIG. 4: Two qutrit analog-digital experiment. (a) Two-qutrit protocol. Evolution of the simulation is achieved by tiling evolution periods of a fixed duration $T_E = 800$ ns interleaved with 60 ns π_{02} pulses on both transmons. Data points in (b) are measured after $2N$ evolution periods. The π_{02} pulses are performed by driving both $|0\rangle \leftrightarrow |1\rangle$ and $|1\rangle \leftrightarrow |2\rangle$ transitions on resonance simultaneously [79, 80]. During each evolution period, in addition to the detuned drives described in Sec. III A, a Stark tone $\Omega_S(t)$ is applied to each transmon, which modifies the entangling Hamiltonian \tilde{H}_{ck} such that the average interaction after two steps is approximately $\tilde{H}_{ck}^{dd} \approx \tilde{z}_{11} L_z \otimes L_z$. (b) Expectation values of L_z (top) and L_z^2 (bottom) for two qutrits during the analog-digital protocol. Dotted lines show exact theory evolution, solid lines are master equation simulations assuming independently measured dephasing and relaxation times. The scale frequency was fixed so that $t_s^{-1} = \tilde{z}_{11}/2\pi \approx 110$ kHz. The initial transmon state was $|\psi_{\text{init}}\rangle_{AB} = |21\rangle$.

with numerically integrated evolution [81] of the Hamiltonian in Eq. (2), as well as a dissipative model described by a Lindbladian that takes into account relaxation and

dephasing times (Table I) of the transmons used in the experiment. We find that the model with decoherence captures the dynamics of the driven system well. To account for the effect of periodic population swaps in the decoherence model with a time-independent master equation, we assume an effective averaged Lindblad equation, where we take the jump operators to be transformed by the periodic application of π_{02} pulses in the same manner as the Hamiltonian. This effective Lindblad model is described in detail in Appendix E. We also plot the transmon eigenstate populations for multiple initial product states along with the predictions of the model in Fig. 14 in the appendix.

IV. GATE-BASED SIMULATION

In this section, we describe the digital gate-based method for simulating the AHM and present the dynamics obtained in experiment. We perform the digital simulation on a Berkeley-based qutrit processor, the properties of which are listed in Table II in Appendix G. The discussion in this section focuses on the mapping of the evolution produced by the AHM to the native gate set of our processor. We also highlight the importance of error mitigation schemes in qutrit simulations for obtaining reliable results with present-day hardware and discuss the associated computational cost.

1. Mapping of the unitary operations to basis gates

For an N_s -qutrit system, the time evolution operator under the model Hamiltonian in Eq. (2) can be approximated using a first-order Trotter approximation,

$$\begin{aligned}
 U(t) &= \exp(-iH_{\text{AHM}}t) \\
 &\simeq \left(\prod_{k=1}^{N_s} M_z^k(\kappa, \delta t) \prod_{k=1}^{N_s-1} M_{zz}^{k,k+1}(\beta, \delta t) \prod_{k=1}^{N_s} M_x^k(\chi, \delta t) \right)^n,
 \end{aligned} \tag{20}$$

where the evolution time t is discretized into uniform steps δt such that $t = n \delta t$. Here, $M_z^k = \exp(-i\theta(L_z^{(k)})^2)$ and $M_x^k = \exp(-i\phi L_x^{(k)})$ denote on-site operations that act on an individual qutrit k , while $M_{zz}^{k,l} = \exp(-i\gamma L_z^{(k)} L_z^{(l)})$ represents an entangling operation between a pair of qutrits k and l . The angles ϕ , θ , and γ are determined by the Hamiltonian parameters χ , κ , and β , as well as the Trotter step duration δt . The matrix representations of these operations are presented in Appendix G. The error in the approximation is bounded by $\mathcal{O}(t \delta t)$. An improved error scaling can be achieved with a higher order Trotter approximation with an increased cost in the number of entangling gates.

To perform the operations M_z^k , M_x^k , and $M_{zz}^{k,l}$ on our superconducting qutrit processor requires further decomposition of the unitaries into our native gate set. In

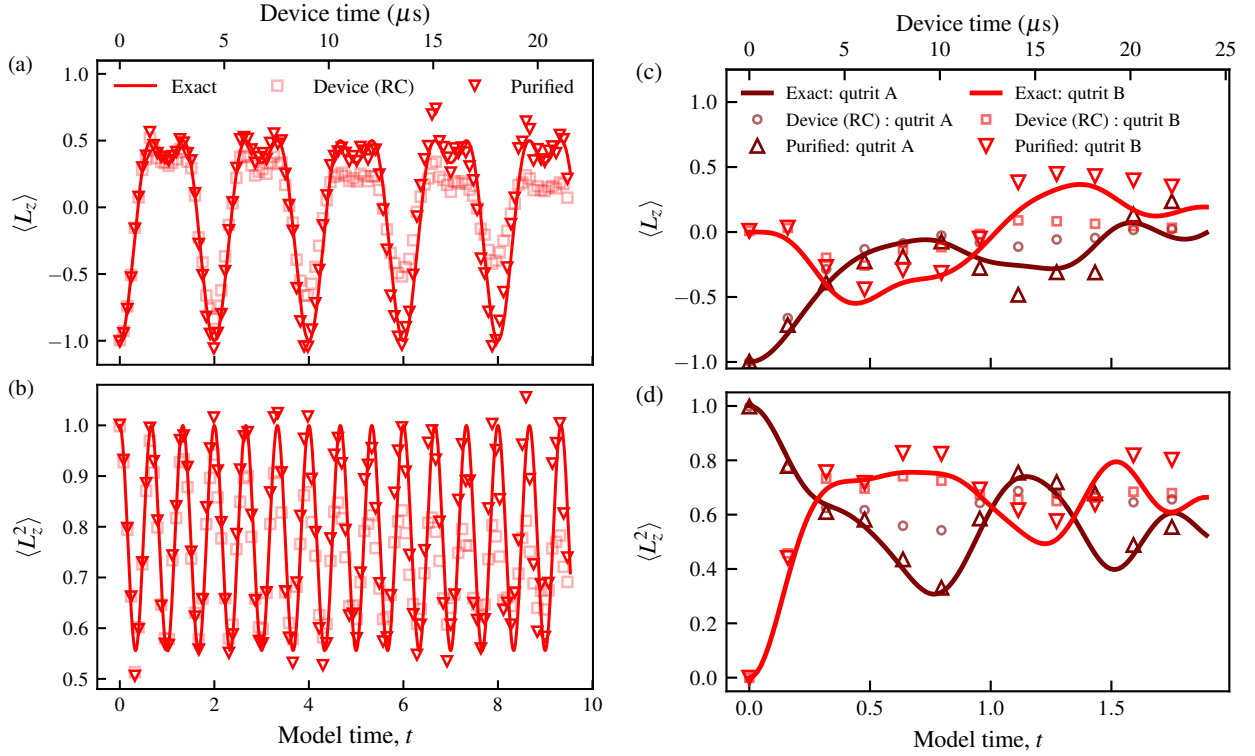


FIG. 5: Exact diagonalization (Exact), device data with randomized compilation (Device (RC)) and error-mitigated device results (Purified) of field operators $\langle L_z \rangle$ and $\langle L_z^2 \rangle$ at (a,b) $\kappa/2\pi = \chi/2\pi = 1.0$ for the single qutrit experiment and (c,d) $\kappa/2\pi = \beta/2\pi = \chi/2\pi = 1.0$ for the two-qutrit experiment. For a discussion on the impact of different types of error mitigation schemes see Appendix H. The dynamics start from the initial state $|\psi_{\text{init}}\rangle_{AB} = |21\rangle$.

contrast to the multi-tone drives used for the analog-digital simulation, we here use single-tone drives that are resonant with a single transition on each transmon qutrit. Such drives can achieve qubit-like rotations in the subspace spanned by either the states $\{|0\rangle, |1\rangle\}$ or $\{|1\rangle, |2\rangle\}$ [62]. The fixed subspace rotations $\{R_x^{01}(\frac{\pi}{2}), R_x^{12}(\frac{\pi}{2}), R_y^{01}(\frac{\pi}{2}), R_y^{12}(\frac{\pi}{2})\}$ and arbitrary phase gates, $R_z^{01}(\theta)$ and $R_z^{12}(\theta)$, which are performed by adjusting the phases of later microwave drives [82], then constitute the native gate set for each qutrit, where we define

$$R_\alpha^{ij}(\theta) = \exp\left(-i\frac{\theta}{2}\sigma_\alpha^{ij}\right), \quad \alpha \in \{x, y, z\}. \quad (21)$$

The σ_α^{ij} are the generators of qubit-like rotations around axis α within the $\{|i\rangle, |j\rangle\}$ subspace of the qutrit Hilbert space and can be expressed in terms of the Gell-Mann matrices (see Appendix G). Then, in combination with the controlled-SUM entangling gate $U_{\text{CSUM}}|i, j\rangle = |i, j+i \pmod{d}\rangle$ we have a gate set that is sufficient for universal qutrit computation [83, 84].

To represent an arbitrary single qutrit operation $\exp(ih)$ using the elementary gates, we first expand h in the Gell-Mann basis $\{\lambda_i\}$, $h = \sum_{k=1}^8 c_k \lambda_k$, where the coefficients are computed with $c_k = \frac{1}{2}\text{Tr}(h\lambda_k)$. Then we perform a first-order Trotter approximation by exponen-

tiating each term in the sum separately. For the M_z^k term this yields an exact decomposition (up to a global phase),

$$M_z(\theta) = R_z^{01}\left(\frac{-2\theta}{3}\right) R_z^{12}\left(\frac{2\theta}{3}\right), \quad (22)$$

where $\theta = (\frac{\kappa}{2} + \beta)\delta t$ for all qutrits except for the boundary qutrits, where instead $\theta = \frac{\kappa+\beta}{2}\delta t$. For the case of $N_s = 2$ studied here, both qutrits are treated as boundary qutrits.

For the M_x^k term, we arrive at an approximate result,

$$M_x(\phi) \simeq R_x^{01}(\sqrt{2}\phi) R_x^{12}(\sqrt{2}\phi), \quad (23)$$

where $\phi = \frac{\chi}{\sqrt{2}}\delta t$. We note that the Trotter approximation in generating the M_x operation could be removed by adding a calibrated $\pi/2$ spin-1 rotation to our digital gate set by applying multitone drives [59, 80], but this is left for future work.

Following a similar analysis, a decomposition for the entangling operation M_{zz} can be found by expressing the two-qutrit Hermitian operator in terms of tensor products of Gell-Mann matrices, $h = \sum_{k,l} c_{kl} \lambda_k \otimes \lambda_l$. This results in four non-zero coefficients. A much simpler decomposition, however, is found by inspection: We decom-

pose the entangling operation M_{zz} into three controlled-SUM gates interleaved with local phase gates,

$$M_{zz}(\gamma) = U_{\text{CSUM}} D(\gamma) U_{\text{CSUM}} G(\gamma) U_{\text{CSUM}} \quad (24)$$

where $\gamma = \delta t \beta$. D and G are diagonal matrices constructed from the elementary phase gates,

$$D(\gamma) = R_z^{01} \left(\frac{4\gamma}{3} \right) R_z^{12} \left(\frac{2\gamma}{3} \right), \quad (25)$$

$$G(\gamma) = R_z^{01} \left(\frac{2\gamma}{3} \right) R_z^{12} \left(\frac{4\gamma}{3} \right). \quad (26)$$

In addition to our circuit decomposition analysis above, we tested whether a more efficient compilation was possible with numerical synthesis methods provided by the TrueQ software [85]. We found comparable costs in entangling operations from numerical synthesis to that of our analytical decomposition. For completeness and a fair comparison with future experiments, a complete set of native gates of the AQT testbed and the key device parameters such as qubit frequencies, anharmonicity, relaxation time and dephasing times are listed in Appendix G.

We find that, for the most efficient decomposition, a single Trotter step of the AHM requires three native entangling gates (Eq. (24)) representing a fourfold reduction compared with the twelve entangling operations needed in the qubit-based implementation with all-to-all connectivity demonstrated in Appendix I. In addition, a restrictive qubit connectivity, like IBM's heavy-hex topology, would roughly increase the cost tenfold (Appendix I). Thus, if the gate times for the native entangling operations, relaxation times and dephasing times of transmon qutrit processors become comparable to state-of-the-art qubit processors, qutrit-based implementations can be favorable for the implementation for certain gauge theory models that inherit $SU(3)$ group structure. This is particularly relevant since $SU(3)$ appears in different limits of QCD [86]. Thus the phase structure of QCD and variants of QCD with various degrees of approximation can likely be studied more efficiently with digital qutrit-based quantum processors [31, 32, 40].

2. Device results

We now present hardware results of our gate-based simulation for the single-site and two-site lattice Abelian Higgs model. In the single-site experiment, the fast high-fidelity single-qutrit gates allow us to observe dynamics for longer times compared to the two-site experiment. Fig. 5 shows error-mitigated hardware results for $\langle L_z^{(k)} \rangle$ and $\langle (L_z^{(k)})^2 \rangle$ expectation values, which are calculated from the measured transmon eigenstate populations, compared with the exact diagonalization and the hardware results with randomized compilation. We find improved fidelity of the circuit operation as we apply qutrit randomized compiling [63, 87–89] to mitigate coherent errors and rescale our expectation values with noise measured from cycle benchmarking [90, 91].

We use 30 distinct twirled versions of the Trotterized circuit where we use $N_{\text{shots}} = 1024$ shots per twirled circuit. Twirling refers to applying local random single-qutrit Pauli operations for each qutrit before and after each cycle of entangling operation. The random operations are selected from the set of generalized Paulis which form an orthogonal basis for a single qutrit. We also employ cycle benchmarking to learn the error rates of different Pauli and SPAM channels associated with the native gates in our circuit, allowing us to correct the observables by post-processing the estimate with a numerical correction factor. Additionally, readout-error mitigation is performed by confusion matrix inversion. The purpose of twirling is to transform coherent noise to stochastic noise channels, which improves the scaling for the accumulation of errors—from quadratic to linear order in circuit depth. This also makes the subsequent mitigation step more effective, as state purification is used to mitigate the incoherent part of the device noise learned from our cycle benchmarking experiments. For a quantitative analysis on the effectiveness of the mitigation schemes, readers are advised to consult the discussion in Appendix H.

V. DISCUSSION AND OUTLOOK

The analog-digital and fully digital approaches to simulating the Abelian Higgs model presented here each have their own potential advantages and remaining challenges. The main strength of performing the simulation on a digital qutrit processor is that it is universal, allowing for

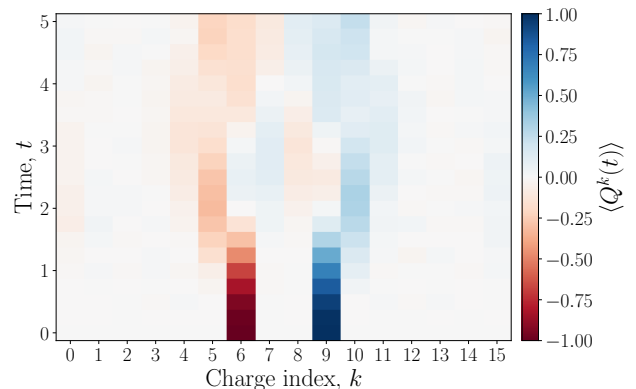


FIG. 6: Demonstration of scalability of the digital simulation protocol with a noiseless simulator [92]. Here we show results of a *Cirq* simulation of the Trotterized unitary in Eq. (20) for a the 15-site lattice model with $\kappa/2\pi = \beta/2\pi = \chi/2\pi = 1.0$. The initial state with two domain walls $|\psi_{\text{init}}\rangle = |111111000111111\rangle$ was prepared and the time-dependence of local charge is computed as the difference in $\langle L_{(z)} \rangle$ between adjacent qutrits: $\langle Q^k(t) \rangle = \langle L_{(z)}^{(k-1)} \rangle - \langle L_{(z)}^{(k)} \rangle$. For open boundary conditions, additional edge sites are assumed to be fixed at $\langle L_z^{(-1)} \rangle = \langle L_z^{(15)} \rangle = 0$ when computing $\langle Q^k \rangle$.

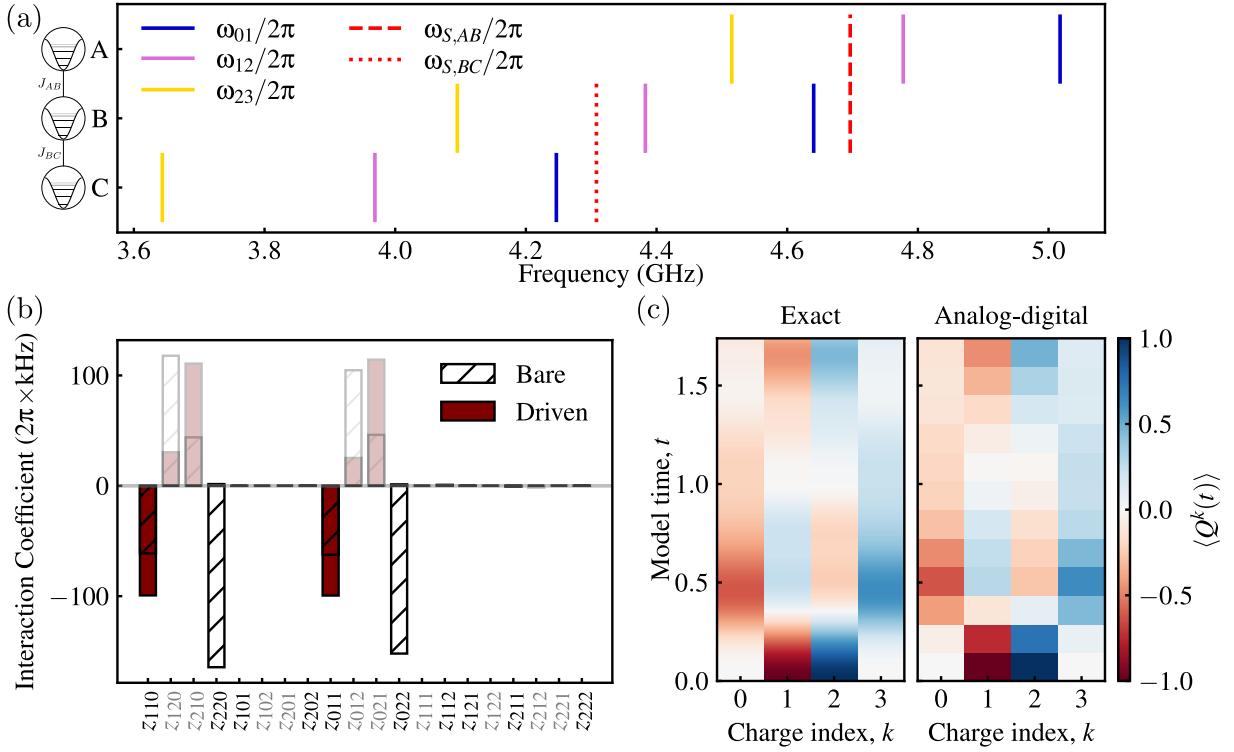


FIG. 7: Verifying the feasibility of scaling up the analog-digital protocol with numerical simulations. (a) Transition frequencies of the three simulated transmons, along with the Stark drive frequencies used to engineer the desired interactions. Note that the transmon-transmon detunings are larger here than in the experiment. Capacitive couplings J_{kl} were set to be $J_{AB} = 2.42$ MHz, $J_{BC} = 2.40$ MHz. (b) Interaction rates of the chain of transmons. In the Bare case (empty hatch), coefficients z_{ijk} are computed from numerical diagonalization of the three-transmon Hamiltonian $H = \sum_{ijk \in \{0,1,2\}} z_{ijk} L_z^i \otimes L_z^j \otimes L_z^k$, where superscripts indicate powers of the L_z operator. In the driven case (maroon), \tilde{z}_{ijk} are calculated by fitting to the phases accumulated after numerically integrating the Schrödinger equation while Stark drives are applied to both pairs of transmons simultaneously. Odd-parity terms under conjugation with U_{02} are grayed out to indicate that they will be canceled by the dynamical decoupling protocol, leaving only $\tilde{z}_{110}/2\pi = -99.3$ kHz and $\tilde{z}_{011}/2\pi = -99.4$ kHz. (c) Numerically simulated evolution of the analog-digital simulation of the AHM on three noiseless transmons with model parameters $\kappa/2\pi = \chi/2\pi = \beta/2\pi = 1$ and a scale frequency $t_s^{-1} = \frac{1}{2\pi}(\tilde{z}_{011} + \tilde{z}_{110})/2$, compared to exact evolution under the AHM. Local charge $\langle Q^k \rangle$ is calculated as the difference in $\langle L_z \rangle$ between adjacent qutrits as in Fig. 6. The initial transmon state was $|\psi_{\text{init}}\rangle = |101\rangle$.

great freedom in varying the model parameters, and in exploring related models, as long as a circuit decomposition may be found. At the same time, the native gate set of the processor may not always permit efficient decompositions of the target operations, as we see here in the need for the Trotterized approximation of the M_x operation and the requirement of three controlled-SUM operations per Trotter step. In contrast, the analog and the analog-digital approaches, while more restrictive in the variety of models they can simulate, demonstrate that it is possible to more directly realize the target Hamiltonian considered here, which was sufficiently close to the device Hamiltonian. In the remainder of this section, we point out some noteworthy aspects of both protocols, and discuss potential directions for future work.

One way these protocols differ is in the immediate availability of error mitigation methods. We have demonstrated that the application of Weyl twirling and purifica-

tion in the digital experiment significantly improves the agreement between the data and the exact diagonalization results. In the analog-digital experiment, however, the same techniques, which rely on the properties of Clifford gates, are not currently available. While there are emerging methods for benchmarking [93–95] and mitigating errors in analog simulations [96–98], they are generally tailored to a particular model or method, and are not yet applicable to the simulation performed here.

When considering scaling up the simulation to longer chains of transmons, the digital protocol may be readily performed on existing devices. Fig. 6 shows numerical simulations of an extension of the digital simulation to a large-scale chain, demonstrating that future experiments with this protocol on near-term qutrit processors may be used to study the dynamics of charges on the lattice and to investigate phenomena such as string breaking and confinement. Scaling up to higher spatial dimensions

will introduce additional engineering challenges and gate costs due to the presence of magnetic field terms, which involve four-body interactions.

Scaling the analog-digital protocol, on the other hand, may require a tailor-made device, due to the requirement that all coupled pairs of transmons have the same effective $L_z \otimes L_z$ interaction rate. We demonstrate in Fig. 7 with numerical simulations that implementing the (1+1)D AHM is possible for an idealized chain of three transmons with one Stark drive per coupled pair, requiring the anharmonicities of the three transmons to be approximately the same, and the detunings between the pairs to also be approximately equal. While this demonstrates that it is possible to scale up the protocol with an appropriately designed device, the frequency spacing requirement is likely too strict for a long chain of fixed-frequency transmons when allowing for fabrication imperfections. To remedy this, one possible avenue is the use of additional Stark drives to modify the interactions further, which we leave for future work.

Although the analog-digital hybrid approach does impose significant constraints on engineering the device, this simultaneous combination of Stark-modified interaction terms, detuned driving, and dynamical decoupling sequences can be thought of as a new tool in the qudit-based analog simulation toolbox, and may enable the construction of hybrid analog-digital simulations of a more diverse range of qudit Hamiltonians. In particular, in conjunction with linear programming methods for robust engineering of qubit [58] and qudit Hamiltonians [54, 59], we may extend to the simulation of models with non-diagonal interaction terms, and on a longer timescale, it may be possible to engineer the magnetic field terms required for the AHM at higher spatial dimensions with proposed analog-digital methods to simulate multi-body interactions [99].

Finally, rather than scaling up the simulation spatially, we may consider increasing the number of states per site. Higher-level quantum operations have been demonstrated on transmons similar to the ones used in this study [100, 101], leaving open the possibility of performing the AHM simulation with a higher level of truncation of the field operators $l \geq 2$ with both digital and analog-digital methods.

VI. CONCLUSION

In summary, we have realized qutrit-based digital and analog-digital hybrid quantum simulations of the Abelian Higgs model on transmon devices and we have demonstrated that they provide a scalable trajectory for simulating lattice gauge theories and spin-1 quantum systems. Our results show that both protocols can extract physical observables relevant to confinement within the coherence limit of present-day transmon processors. Despite the additional challenges associated with controlling more levels and more complicated interaction Hamil-

tonians, the qutrit-based experiments performed in this work allowed for a more hardware-efficient encoding of the spin-1 model than a qubit-based simulation, requiring fewer entangling operations.

While the nature of this study does not admit a quantitative comparison between the two methods, tools developed in this work can be used for a quantitative resource analysis of the two protocols for different lattice field theory models in the future. The analog-digital protocol developed here is scalable with minimal modification whereas the digital protocol with error mitigation methods is scalable without any further modification. We find that scaling up the analog-digital protocol practically introduces more constraints, but has the potential to reduce the total number of pulses required for the simulation. An exciting next step would be to investigate string breaking and confinement phenomena in more spatial dimensions, as well as approaching a higher-order approximation of the base theory with higher-dimensional qudits.

ACKNOWLEDGMENTS

We would like to thank Gabriel T. Landi for helpful discussions on the Lindblad master equation. MA and AFK were supported by the U.S. Department of Energy, Advanced Scientific Computing Research, under contract number DE-SC0025430. YM and ZO were supported in part by the Dept. of Energy under Award Number DE-SC0019139. RWP, AIM, and MSB were supported by the U.S. Department of Energy, award No. DE-SC0024714. NG was supported by the U.S. Department of Energy, Office of Science, Office of Advanced Scientific Computing Research Quantum Testbed Program under contract DE-AC02-05CH11231. Devices used in the analog-digital hybrid experiment were fabricated and provided by the Superconducting Qubits at Lincoln Laboratory (SQUILL) Foundry at MIT Lincoln Laboratory, with funding from the Laboratory for Physical Sciences (LPS) Qubit Collaboratory. The traveling-wave parametric amplifier (TWPA) used in the analog-digital hybrid experiment was provided by IARPA and Lincoln Labs.

Appendix A: Average Hamiltonian Theory

For complete reviews of Average Hamiltonian Theory (AHT), see, e.g., [70, 102]. Here, for convenience, we briefly summarize the key ideas and present the results that are relevant to the development of our simulation protocols.

A unitary operator $U(t, t_0)$ can be written as the matrix exponential of some Hermitian operator Θ_{t, t_0} : $U(t, t_0) = \exp(i\Theta_{t, t_0})$ [103, 104]. This implies that, for an arbitrary time-dependent Hamiltonian $H(t)$ that gen-

erates $U(t_f, t_0)$ over the fixed interval $[t_0, t_f]$ by

$$U(t_f, t_0) = \hat{\mathcal{T}} \exp \left(-i \int_{t_0}^{t_f} H(t') dt' \right), \quad (\text{A1})$$

where $\hat{\mathcal{T}} \exp(\cdot)$ is the time-ordered exponential, we may define some time-independent Hamiltonian \bar{H}_{t_f, t_0} such that

$$U(t_f, t_0) = \exp(-iT\bar{H}_{t_f, t_0}), \quad (\text{A2})$$

where $T = t_f - t_0$. Assuming conditions of convergence apply, the Hamiltonian \bar{H}_{t_f, t_0} may be expressed with the Magnus expansion [103, 104]

$$\bar{H} = \sum_{n=1}^{\infty} \bar{H}^{(n)}, \quad (\text{A3})$$

where the first three terms are

$$\bar{H}^{(1)} = \frac{1}{T} \int_{t_1=t_0}^{t_f} H(t_1) dt_1, \quad (\text{A4})$$

$$\bar{H}^{(2)} = \frac{1}{2iT} \int_{t_1=t_0}^{t_f} \int_{t_2=t_0}^{t_1} [H(t_1), H(t_2)] dt_2 dt_1, \quad (\text{A5})$$

$$\begin{aligned} \bar{H}^{(3)} = & \frac{-1}{6T} \int_{t_1=t_0}^{t_f} \int_{t_2=t_0}^{t_1} \int_{t_3=t_0}^{t_2} \left([H(t_1), [H(t_2), H(t_3)]] \right. \\ & \left. + [[H(t_1), H(t_2)], H(t_3)] \right) dt_3 dt_2 dt_1. \end{aligned} \quad (\text{A6})$$

Truncating the series at a finite order yields an *effective average Hamiltonian* $\bar{H}_{\text{eff}} = \sum_{n=1}^m \bar{H}^{(n)} \approx \bar{H}$.

Each successive order of the average Hamiltonian involves increasingly nested commutators of $H(t)$ with itself at different times. Hence, if the Hamiltonian commutes with itself at all times,

$$[H(t_1), H(t_2)] = 0 \quad \forall t_1, t_2 \in [t_0, t_f],$$

then $\bar{H}^{(n)} = 0$ for $n \geq 2$ and the expansion is exact at the first order.

Another property of the expansion that aids in the development of our simulation protocol is the fact that a symmetric Hamiltonian, where $H(t) = H(t_f - (t - t_0))$ for all $t \in [t_0, t_f]$, will yield exactly zero for all even-ordered terms in the expansion, that is, $\bar{H} = \bar{H}^{(1)} + \bar{H}^{(3)} + \dots$ [70].

Lastly, given a sequence of time-independent Hamiltonians $\{H_1, H_2, \dots, H_N\}$, or, as in the case of the analog-digital protocol, a Hamiltonian where the evolution is driven in pulsed segments that can themselves be approximated by time-independent Hamiltonians with AHT, the integrals above can be replaced by sums:

$$\bar{H}_{\text{disc}}^{(1)} = \frac{1}{N} \sum_{i=1}^N H_i, \quad (\text{A7})$$

$$\bar{H}_{\text{disc}}^{(2)} = \frac{1}{2iN} \sum_{i=2}^N \sum_{j=1}^{i-1} [H_i, H_j] T, \quad (\text{A8})$$

where we have omitted the third order term for simplicity, and where we have assumed that all Hamiltonians in the sequence are active for the same duration T . The ‘‘disc’’ suffix is only to distinguish this discrete average Hamiltonian from the integral definitions above.

Appendix B: Analog Detuned Drive Rotating Frame Transformation and Phase Ramping Derivation

In the analog protocol, the driven transmon Hamiltonian approximates the Abelian Higgs Hamiltonian in the frame of the drive, after accounting for the fact that the drive frequency is time-dependent. This appendix expands on the transformation into the drive frame and derives the phase ramping required to produce an instantaneous detuning with a particular envelope. We start with the lab frame Hamiltonian of the driven transmon, truncated to three levels:

$$\begin{aligned} H_k^{\text{LF}}(t) &= H_k^0 + H_k^{\text{drive}}(t) \\ &= \omega_{01} |1\rangle\langle 1| + (\omega_{01} + \omega_{12}) |2\rangle\langle 2| \\ &\quad + V(t) (i |1\rangle\langle 0| + i\lambda |2\rangle\langle 1| + \text{h.c.}). \end{aligned} \quad (\text{B1})$$

For time-independent detunings, $V(t)$ may be defined as in the main text, $V(t) = \sum_{i=1}^2 \Omega_i(t) \cos(\omega_i^{\text{d}} t + \phi_i) = \sum_{i=1}^2 \Omega_i(t) \cos((\omega_{i-1, i} - \Delta_i) t + \phi_i)$. Here we use a more general expression,

$$V(t) = \sum_{i=1}^2 \Omega_i(t) \cos(\omega_{i-1, i} t + \delta\phi_i(t) + \phi_i), \quad (\text{B2})$$

where the (now potentially time-dependent) detuning has been absorbed into a time-dependent phase. The rotating frame transformation is defined in a similar manner to the time-independent case:

$$H^{\text{DF}} = U_{\text{D}}^{\dagger} H^{\text{LF}} U_{\text{D}} - i U_{\text{D}}^{\dagger} \partial_t U_{\text{D}}, \quad (\text{B3})$$

where now

$$U_{\text{D}}(t) = \begin{pmatrix} 1 & 0 & 0 \\ 0 & e^{-i(\omega_{01} t + \delta\phi_1(t))} & 0 \\ 0 & 0 & e^{-i((\omega_{01} + \omega_{12}) t + \delta\phi_1(t) + \delta\phi_2(t))} \end{pmatrix}. \quad (\text{B4})$$

This produces the following rotated Hamiltonian, without taking the RWA:

$$\begin{aligned}
H_k^{\text{DF}}(t) &= (\omega_{01} - \delta\dot{\phi}_1) |1\rangle\langle 1| + (\omega_{01} + \omega_{12} - \delta\dot{\phi}_1 - \delta\dot{\phi}_2) |2\rangle\langle 2| \\
&\quad + \frac{i}{2} \left(\Omega_1 e^{-i\phi_1} + \Omega_1 e^{2i(\omega_{01}t + \delta\phi_1(t)) + i\phi_1} \right. \\
&\quad\quad\quad + \Omega_2 e^{i(\omega_{01}t + \delta\phi_1(t) + \omega_{12}t + \delta\phi_2(t)) + i\phi_2} \\
&\quad\quad\quad \left. + \Omega_2 e^{i(\omega_{01}t + \delta\phi_1(t) - \omega_{12}t - \delta\phi_2(t)) - i\phi_2} \right) |1\rangle\langle 0| \\
&\quad + \frac{i\lambda}{2} \left(\Omega_2 e^{-i\phi_2} + \Omega_2 e^{2i(\omega_{12}t + \delta\phi_2(t)) + i\phi_2} \right. \\
&\quad\quad\quad + \Omega_1 e^{i(\omega_{12}t + \delta\phi_2(t) + \omega_{01}t + \delta\phi_1(t)) + i\phi_1} \\
&\quad\quad\quad \left. + \Omega_1 e^{i(\omega_{12}t + \delta\phi_2(t) - \omega_{01}t - \delta\phi_1(t)) - i\phi_1} \right) |2\rangle\langle 1| + \text{h.c.}
\end{aligned}$$

The oscillating terms involving the sums of frequencies ω_{01} and ω_{12} may be dropped safely under the same conditions as the standard RWA, assuming $\Omega \ll \omega_{01} + \omega_{12} \approx 2\omega_{01}$. The terms involving the difference of the two frequencies, however, introduce a stricter condition for the RWA: $\Omega \ll |\omega_{01} - \omega_{12}|$ (where we have already required that the oscillation due to the $\delta\phi(t)$ terms is small because the detunings must be much smaller than the magnitude of the anharmonicity). In the experiments presented here, we have $\Omega/|\omega_{01} - \omega_{12}| \sim 4 \times 10^{-3}$ in the single-qutrit experiment and $\Omega/|\omega_{01} - \omega_{12}| \sim 4 \times 10^{-4}$ in the two-qutrit experiment, which both meet the stricter RWA requirement. When the RWA conditions are met, all oscillating terms may be dropped and the rotating frame Hamiltonian may be approximated as

$$\begin{aligned}
H_k^{\text{DF}}(t) &\approx (\omega_{01} - \delta\dot{\phi}_1) |1\rangle\langle 1| \\
&\quad + (\omega_{01} + \omega_{12} - \delta\dot{\phi}_1 - \delta\dot{\phi}_2) |2\rangle\langle 2| \\
&\quad - \frac{i}{2} \Omega_1 |0\rangle\langle 1| - \frac{i\lambda}{2} \Omega_2 |1\rangle\langle 2| + \text{h.c.}
\end{aligned} \tag{B5}$$

The derivatives of the phase accumulation functions can be seen to play the same role as the detunings in the time-independent case, Eq. (8), so we may define $\Delta_i(t) = \delta\dot{\phi}_i(t)$ to obtain,

$$\begin{aligned}
H_k^{\text{DF}}(t) &\approx -\Delta_1(t) |1\rangle\langle 1| - (\Delta_1(t) + \Delta_2(t)) |2\rangle\langle 2| \\
&\quad + \frac{i}{2} \Omega_1 |0\rangle\langle 1| + \frac{i\lambda}{2} \Omega_2 |1\rangle\langle 2| + \text{h.c.}
\end{aligned} \tag{B6}$$

This implies that, given a desired $\Delta(t)$, we must ramp the phase on the drives according to $\delta\phi(t) = \int_0^t \Delta(t') dt'$ [105]. Further, for a sequence of pulses, we find that to maintain a consistent phase reference with the detuned frame we must ensure that the phase accumulations $\delta\phi(t)$ are maintained from the end of one pulse to the start of the next.

The envelope function used for both the analog pulses and the π_{02} gates was a flat-topped pulse with a cosine-

shaped rise and fall, given by

$$A_T(t) = \begin{cases} a \sin^2\left(\frac{\pi t}{2rT}\right), & 0 \leq t < rT \\ a, & rT \leq t < (1-r)T \\ a \sin^2\left(\frac{\pi(T-t)}{2rT}\right), & (1-r)T \leq t \leq T, \end{cases} \tag{B7}$$

where r is the fraction of the pulse each ramp occupies and a is the normalization factor $1/(1-r)$, which results in a total area of $\int_0^T A_T(t) dt = T$. For the π_{02} gates, we also incorporated a second-order DRAG correction [106] to reduce the effects of off-resonant excitations.

Appendix C: Dispersive Interaction Rate Calculations

The effective dispersive interaction between two capacitively coupled transmon qutrits may be approximately derived from the time independent bare system Hamiltonian,

$$H_{\text{sys}} = H_A^0 + H_B^0 + H_{AB}, \tag{C1}$$

where H_A^0 and H_B^0 are the bare Hamiltonians of transmons A and B , respectively, and $H_{AB} = J\hat{n}_A\hat{n}_B \approx J(\hat{a}_A\hat{a}_B^\dagger + \hat{a}_A^\dagger\hat{a}_B)$ represents the bare capacitive coupling, where we have already taken the rotating wave approximation, with $\hat{a}_k^\dagger = \sum_{i=1}^d \mu_{k,i} |i\rangle\langle i-1|$, the raising operator for the energy eigenstates of transmon $k \in \{A, B\}$ with dimensionless charge matrix elements $\mu_{k,i} \approx \sqrt{i}$ [47]. In practice, we do not use the \sqrt{i} approximation, and instead use values calculated from numerical diagonalization of the transmon Hamiltonian [107, 108].

We may use second-order time-independent perturbation theory [109] to approximately diagonalize the two-transmon Hamiltonian \hat{H}_{sys} and arrive at the effective energy level shifts in the absence of any drive. Note that we must take both transmon Hamiltonians to at least eigenstate $|3\rangle$ (four level approximation) for accurate estimates of the shifts on the first three levels. The diago-

nalized Hamiltonian may be expressed generally as

$$H_{\text{sys}} \approx H_A^0 + H_B^0 + \sum_{i,j=0}^{d-1} \varepsilon_{i,j} |ij\rangle\langle ij|. \quad (\text{C2})$$

After absorbing the shifts that correspond to redefining the transition frequencies of each of the two transmons into $H_A^0 \rightarrow H_A^{0'}$ and $H_B^0 \rightarrow H_B^{0'}$, we arrive at

$$H_{\text{sys}} \approx H_A^{0'} + H_B^{0'} + H_{\text{ck}}, \quad (\text{C3})$$

with the cross-Kerr interaction Hamiltonian,

$$H_{\text{ck}} = \alpha_{11}^0 |11\rangle\langle 11| + \alpha_{12}^0 |12\rangle\langle 12| + \alpha_{21}^0 |21\rangle\langle 21| + \alpha_{22}^0 |22\rangle\langle 22|, \quad (\text{C4})$$

with rates given by the perturbation theory:

$$\alpha_{11}^0 = J^2 \left(\frac{\mu_{A,1}^2 \mu_{B,2}^2}{\omega_1^A - \omega_2^B} - \frac{\mu_{A,2}^2 \mu_{B,1}^2}{\omega_2^A - \omega_1^B} \right) \quad (\text{C5})$$

$$\alpha_{12}^0 = -J^2 \left(\frac{\mu_{A,2}^2 \mu_{B,2}^2}{\omega_2^A - \omega_2^B} + \mu_{A,1}^2 \left(\frac{\mu_{B,1}^2}{\omega_1^A - \omega_1^B} - \frac{\mu_{B,2}^2}{\omega_1^A - \omega_2^B} - \frac{\mu_{B,3}^2}{\omega_1^A - \omega_3^B} \right) \right) \quad (\text{C6})$$

$$\alpha_{21}^0 = J^2 \left(\frac{\mu_{A,2}^2 \mu_{B,2}^2}{\omega_2^A - \omega_2^B} + \mu_{B,1}^2 \left(\frac{\mu_{A,1}^2}{\omega_1^A - \omega_1^B} - \frac{\mu_{A,2}^2}{\omega_2^A - \omega_1^B} - \frac{\mu_{A,3}^2}{\omega_3^A - \omega_1^B} \right) \right) \quad (\text{C7})$$

$$\alpha_{22}^0 = -J^2 \left(\mu_{A,2}^2 \left(\frac{\mu_{B,1}^2}{\omega_2^A - \omega_1^B} - \frac{\mu_{B,3}^2}{\omega_2^A - \omega_3^B} \right) - \mu_{B,2}^2 \left(\frac{\mu_{A,1}^2}{\omega_1^A - \omega_2^B} - \frac{\mu_{A,3}^2}{\omega_3^A - \omega_2^B} \right) \right). \quad (\text{C8})$$

For the sake of visual simplicity, in this section we represent the transition frequency between levels $i-1$ and i as $\omega_i \equiv \omega_{i-1,i}$.

To modify the interaction rates, we use Stark drives at frequency ω_S applied to both qutrits. This method has been used to produce controlled-Z gates in both superconducting qubit [110, 111] and qutrit devices [78]. For convenience, we review the perturbation analysis of the method here.

We start with a two-transmon Hamiltonian in the lab frame with Stark drives on both transmons,

$$\tilde{H}_{\text{sys}}^{\text{LF}} = H_A^0 + H_A^{\text{Stark}}(t) + H_B^0 + H_B^{\text{Stark}}(t) + H_{AB}, \quad (\text{C9})$$

where the Stark drive Hamiltonian for each transmon, assuming the rotating wave approximation from the outset, is given by

$$\begin{aligned} H_k^{\text{Stark}}(t) &= i\Omega_{S,k}^0 \cos(\omega_S t + \phi_k) (\hat{a}_k^\dagger - \hat{a}_k) \\ &\approx i \frac{\Omega_{S,k}^0}{2} \left(e^{-i(\omega_S t + \phi_k)} \hat{a}_k^\dagger - e^{i(\omega_S t + \phi_k)} \hat{a}_k \right). \end{aligned} \quad (\text{C10})$$

We may obtain a time-independent RWA Hamiltonian by rotating into the frame of the drive on both transmons with $U_S = U_{S,A} \otimes U_{S,B}$ and $U_{S,k} = \sum_{n=0}^d e^{in\omega_S t} |n\rangle\langle n|$, arriving at a time-independent Hamiltonian in the frame of the Stark drive,

$$\begin{aligned} \tilde{H}_{\text{sys}}^{\text{SF}} &\approx \left(\sum_{i=1}^d \epsilon_i^A |i\rangle\langle i| \right) \otimes I + I \otimes \left(\sum_{j=1}^d \epsilon_j^B |j\rangle\langle j| \right) \\ &+ \left(i \sum_{i=1}^d \mu_{A,i} \frac{\Omega_{S,A}^0 e^{-i\phi_A}}{2} |i\rangle\langle i-1| \right) \otimes I \\ &+ I \otimes \left(i \sum_{j=1}^d \mu_{B,j} \frac{\Omega_{S,B}^0 e^{-i\phi_B}}{2} |j\rangle\langle j-1| \right) \\ &+ J \sum_{i,j=1}^d \mu_{A,i} \mu_{B,j} |i\rangle\langle i-1| \otimes |j-1\rangle\langle j| + \text{h.c.}, \end{aligned} \quad (\text{C11})$$

where we define $\epsilon_j^k \equiv \sum_{j'=1}^j (\omega_{j'}^k - \omega_S) = \sum_{j'=1}^j \Delta_{j'}^k$, and $\Delta_i^k \equiv \omega_{i-1,i}^k - \omega_S$. That is, the effective energy terms in the rotated frame are the cumulative sums of the detunings of each successive transition from the Stark drive frequency.

The Hamiltonian may now be perturbatively diagonalized to third order, and then rotated back to the lab frame with the inverse transformation U_S^\dagger , resulting in an effectively diagonal Hamiltonian with modified interaction rates and Stark-shifted transition frequencies on both transmons,

$$\tilde{H}_{\text{sys}}^{\text{LF}} \approx \tilde{H}_A^{0'} + \tilde{H}_B^{0'} + \tilde{H}_{\text{ck}}. \quad (\text{C12})$$

The coefficients in the modified interaction Hamiltonian

\tilde{H}_{ck} are

$$\tilde{\alpha}_{11} = J\Omega_{S,A}^0\Omega_{S,B}^0 \cos(\delta\phi) \left\{ \frac{\mu_{A,1}^2}{\Delta_1^A} \left(\frac{2\mu_{B,1}^2}{\Delta_1^B} - \frac{\mu_{B,2}^2}{\Delta_2^B} \right) - \frac{\mu_{A,2}^2}{2\Delta_2^A} \left(\frac{2\mu_{B,1}^2}{\Delta_1^B} - \frac{\mu_{B,2}^2}{\Delta_2^B} \right) \right\} + \alpha_{11}^0 \quad (\text{C13})$$

$$\tilde{\alpha}_{12} = J\Omega_{S,A}^0\Omega_{S,B}^0 \cos(\delta\phi) \left\{ \frac{\mu_{A,1}^2}{\Delta_1^A} \left(\frac{\mu_{B,1}^2}{\Delta_1^B} + \frac{\mu_{B,2}^2}{\Delta_2^B} - \frac{\mu_{B,3}^2}{\Delta_3^B} \right) - \frac{\mu_{A,2}^2}{2\Delta_2^A} \left(\frac{\mu_{B,1}^2}{\Delta_1^B} + \frac{\mu_{B,2}^2}{\Delta_2^B} - \frac{\mu_{B,3}^2}{\Delta_3^B} \right) \right\} + \alpha_{12}^0 \quad (\text{C14})$$

$$\tilde{\alpha}_{21} = J\Omega_{S,A}^0\Omega_{S,B}^0 \cos(\delta\phi) \left\{ \frac{\mu_{B,1}^2}{\Delta_1^B} \left(\frac{\mu_{A,1}^2}{\Delta_1^A} + \frac{\mu_{A,2}^2}{\Delta_2^A} - \frac{\mu_{A,3}^2}{\Delta_3^A} \right) - \frac{\mu_{B,2}^2}{2\Delta_2^B} \left(\frac{\mu_{A,1}^2}{\Delta_1^A} + \frac{\mu_{A,2}^2}{\Delta_2^A} - \frac{\mu_{A,3}^2}{\Delta_3^A} \right) \right\} + \alpha_{21}^0 \quad (\text{C15})$$

$$\tilde{\alpha}_{22} = J\Omega_{S,A}^0\Omega_{S,B}^0 \cos(\delta\phi) \left\{ \frac{\mu_{A,1}^2}{2\Delta_1^A} \left(\frac{\mu_{B,1}^2}{\Delta_1^B} + \frac{\mu_{B,2}^2}{\Delta_2^B} - \frac{\mu_{B,3}^2}{\Delta_3^B} \right) + \frac{\mu_{A,2}^2}{2\Delta_2^A} \left(\frac{\mu_{B,1}^2}{\Delta_1^B} + \frac{\mu_{B,2}^2}{\Delta_2^B} - \frac{\mu_{B,3}^2}{\Delta_3^B} \right) - \frac{\mu_{A,3}^2}{2\Delta_3^A} \left(\frac{\mu_{B,1}^2}{\Delta_1^B} + \frac{\mu_{B,2}^2}{\Delta_2^B} - \frac{\mu_{B,3}^2}{\Delta_3^B} \right) \right\} + \alpha_{22}^0, \quad (\text{C16})$$

where $\delta\phi$ is the phase difference between the Stark drives, $\delta\phi = \phi_A - \phi_B$. The local frequency shifts in $\tilde{H}_k^{0'}$ are the standard AC-Stark shifts [112] of a multilevel ladder-type system subjected to an off-resonant drive at ω_S , that is, $\tilde{\omega}_{i-1,i}^S = \omega_{i-1,i} + \delta_{i-1,i}^S$, where

$$\delta_{i-1,i}^S = \frac{-1}{4} \frac{\mu_{i-1}^2 \Omega_S^2}{\Delta_{i-1}} + \frac{1}{2} \frac{\mu_i^2 \Omega_S^2}{\Delta_i} - \frac{1}{4} \frac{\mu_{i+1}^2 \Omega_S^2}{\Delta_{i+1}},$$

and we take $\mu_0 \equiv 0$. We measure these local shifts with Ramsey experiments and compensate for them by adjusting the detunings of the on-site simulation drives.

Given the above expressions for $\tilde{\alpha}_{ij}(\Omega_{S,A}^0, \Omega_{S,B}^0, \omega_S, \delta\phi)$, we now perform a transformation of variables to simplify the engineering of the desired $L_z \otimes L_z$ interaction Hamiltonian. For convenience, we will use an intermediate representation that better respects the structure of the target Hamiltonian. By analogy with the definition of the α_{ij} in terms of the energy levels of the two-transmon system, $\alpha_{ij} = (\varepsilon_{ij} - \varepsilon_{i0}) - (\varepsilon_{0j} - \varepsilon_{00})$, we may define instead $\zeta_{ij} = (\varepsilon_{ij} - \varepsilon_{i1}) - (\varepsilon_{1j} - \varepsilon_{11})$, which contain the same information as the α_{ij} , but reference energy levels from the $|11\rangle$ state, rather than the $|00\rangle$ state of the two-transmon system. By substituting the expressions for α_{ij} into this definition, we find four nonzero ζ_{ij} :

$$\begin{aligned} \zeta_{00} &= \alpha_{11} \\ \zeta_{02} &= \alpha_{11} - \alpha_{12} \\ \zeta_{20} &= \alpha_{11} - \alpha_{21} \\ \zeta_{22} &= (\alpha_{22} - \alpha_{21}) - (\alpha_{12} - \alpha_{11}). \end{aligned} \quad (\text{C17})$$

This procedure effectively redefines the transition frequencies of the individual transmons, as outlined in the main text, and results in a Hamiltonian that is equivalent

to that given in Eq. (14), represented in a different basis:

$$H'_{\text{ck}} = \zeta_{00} |00\rangle\langle 00| + \zeta_{02} |02\rangle\langle 02| + \zeta_{20} |20\rangle\langle 20| + \zeta_{22} |22\rangle\langle 22|. \quad (\text{C18})$$

From here, it is a matter of inspection to define the z_{ij} coefficients in terms of the ζ_{ij} and hence the α_{ij} . This relationship may be represented by the matrix equation,

$$\begin{pmatrix} z_{11} \\ z_{12} \\ z_{21} \\ z_{22} \end{pmatrix} = \frac{1}{4} \begin{pmatrix} 1 & -1 & -1 & 1 \\ 1 & 1 & -1 & -1 \\ 1 & -1 & 1 & -1 \\ 1 & 1 & 1 & 1 \end{pmatrix} \begin{pmatrix} \zeta_{00} \\ \zeta_{02} \\ \zeta_{20} \\ \zeta_{22} \end{pmatrix}. \quad (\text{C19})$$

To identify candidate Stark drive frequencies and amplitudes, we perform a numerical search for zero crossings with the perturbation theory expression for the driven $\tilde{z}_{22}(\Omega_{S,A}^0, \Omega_{S,B}^0, \omega_S, \delta\phi)$. We simplify the parameter space by restricting $\delta\phi$ to two values $\delta\phi \in \{0, \pi\}$, and by requiring that $\Omega_{S,A}^0 = \Omega_{S,B}^0 = \Omega_S^0$. We find that for the two transmons used here (in the straddling regime), there exist several ranges of frequencies that admit $\tilde{z}_{22} = 0$ for a given drive amplitude. As can be seen in Fig. 8, we see the strongest response in \tilde{z}_{22} when $\omega_{12}^B < \omega_S < \omega_{12}^A$. We find that the perturbation theory results agree at least qualitatively with the experiment when not driving too close to any transition frequencies, and are therefore a useful starting point for the calibration. Experimental calibration of the amplitudes is described in Appendix D, see Fig. 10(b).

Appendix D: Entangling Rate Measurement Protocols

To measure the coefficients of the entangling Hamiltonian experimentally, we use a series of modified

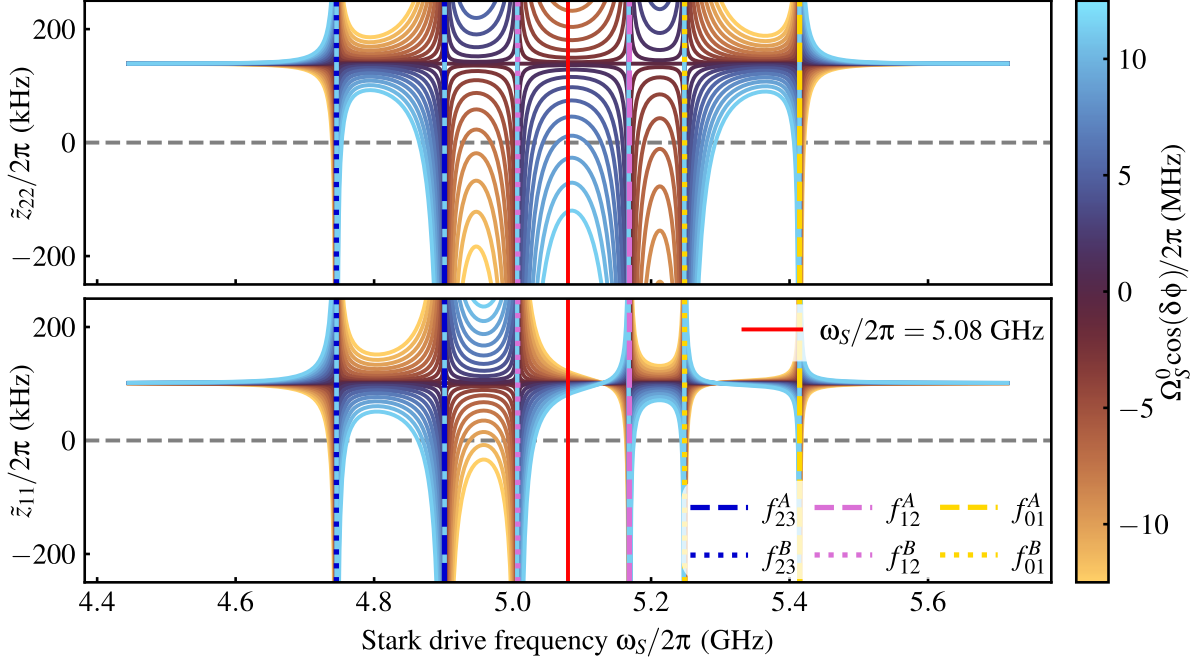


FIG. 8: Third-order perturbation theory results for the driven interaction rates, based on the experimentally measured spectra of the two transmons used in the analog-digital experiment, plotted vs frequency $k \in \{A, B\}$, $f_{ij}^k = \omega_{ij}^k/2\pi$, are marked with vertical lines. Expressions for the driven rates $\tilde{z}_{11}(\Omega_S^0, \omega_S, \delta\phi)$ and $\tilde{z}_{22}(\Omega_S^0, \omega_S, \delta\phi)$ can be obtained from Eqs. (C13)–(C16). The solid red vertical line indicates the frequency of the Stark drive used in this experiment.

JAZZ/BIRD sequences [75, 76] that can both extract the individual entangling rates and decouple from small transition frequency offsets produced by miscalibration or slow drifts.

For two qutrits, each entangling rate ζ_{ij} ($i, j \in \{0, 2\}$)—defined in Eq. (C18) and related to the original cross-Kerr entangling rates α_{ij} ($i, j \in \{1, 2\}$) in Eq. (C17)—may be extracted from the Ramsey oscillations of an individual JAZZ sequence, as shown in Fig. 9, where the sequences for different i, j only differ by the choice of subspace for the $\pi/2$ pulses and the π pulses that echo any unconditional frequency shifts.

To unambiguously determine the sign of the JAZZ Ramsey frequencies, we add an “artificial detuning” δ_{art} to the Ramsey sequence by varying the phase of the final $\pi/2$ pulse as $\theta(T) = \pm\delta_{\text{art}}T$, where T is the (varying) duration of each evolution period in the sequence [113], and we perform each JAZZ Ramsey experiment twice: once with $+\delta_{\text{art}}$, and once with $-\delta_{\text{art}}$. Specific to this particular decoupling pulse protocol, the sign of the measured JAZZ Ramsey frequencies is reversed for $i = 2$, which must be compensated for.

The frequency of oscillation in a single JAZZ measurement for a particular ζ_{ij} is then $\omega_{\text{JAZZ},0j}^{\pm} = |\pm\delta_{\text{art}} - \zeta_{0j}|$ for $i = 0$ or $\omega_{\text{JAZZ},2j}^{\pm} = |\pm\delta_{\text{art}} + \zeta_{2j}|$ for $i = 2$. Under the assumption that the magnitude of the artificial detuning is larger than the magnitude of the frequency to be

measured, the signed entangling rate may be estimated by,

$$\zeta_{ij} = \begin{cases} \frac{\omega_{\text{JAZZ},ij}^- - \omega_{\text{JAZZ},ij}^+}{2}, & i = 0 \\ \frac{\omega_{\text{JAZZ},ij}^+ - \omega_{\text{JAZZ},ij}^-}{2}, & i = 2 \end{cases} \quad (\text{D1})$$

Individual JAZZ Ramsey measurement results for the driven rates $\tilde{\zeta}_{ij}$ are shown in Fig. 9 below each corresponding circuit diagram.

In addition, the more complicated sequence given in Fig. 10(a), with eight periods of evolution, may be shown to produce oscillations at the sum of the ζ_{ij} interaction rates, providing an estimate of $z_{22} = \frac{1}{4}(\zeta_{00} + \zeta_{02} + \zeta_{20} + \zeta_{22})$ in a single experiment. This allows for efficient calibration of the Stark drive amplitudes required to produce the condition $z_{22} = 0$, as shown in Fig. 10(b).

Finally, to calibrate the local frequency shifts produced by the Stark drives on the two transmons, we perform simple Ramsey experiments on each transition of each transmon with the Stark drive active during the wait period. These measurements are performed while the other transmon is in the $|1\rangle$ state, to directly provide the frequencies required by the frame shift of Eq. (14) and also described in Appendix C.

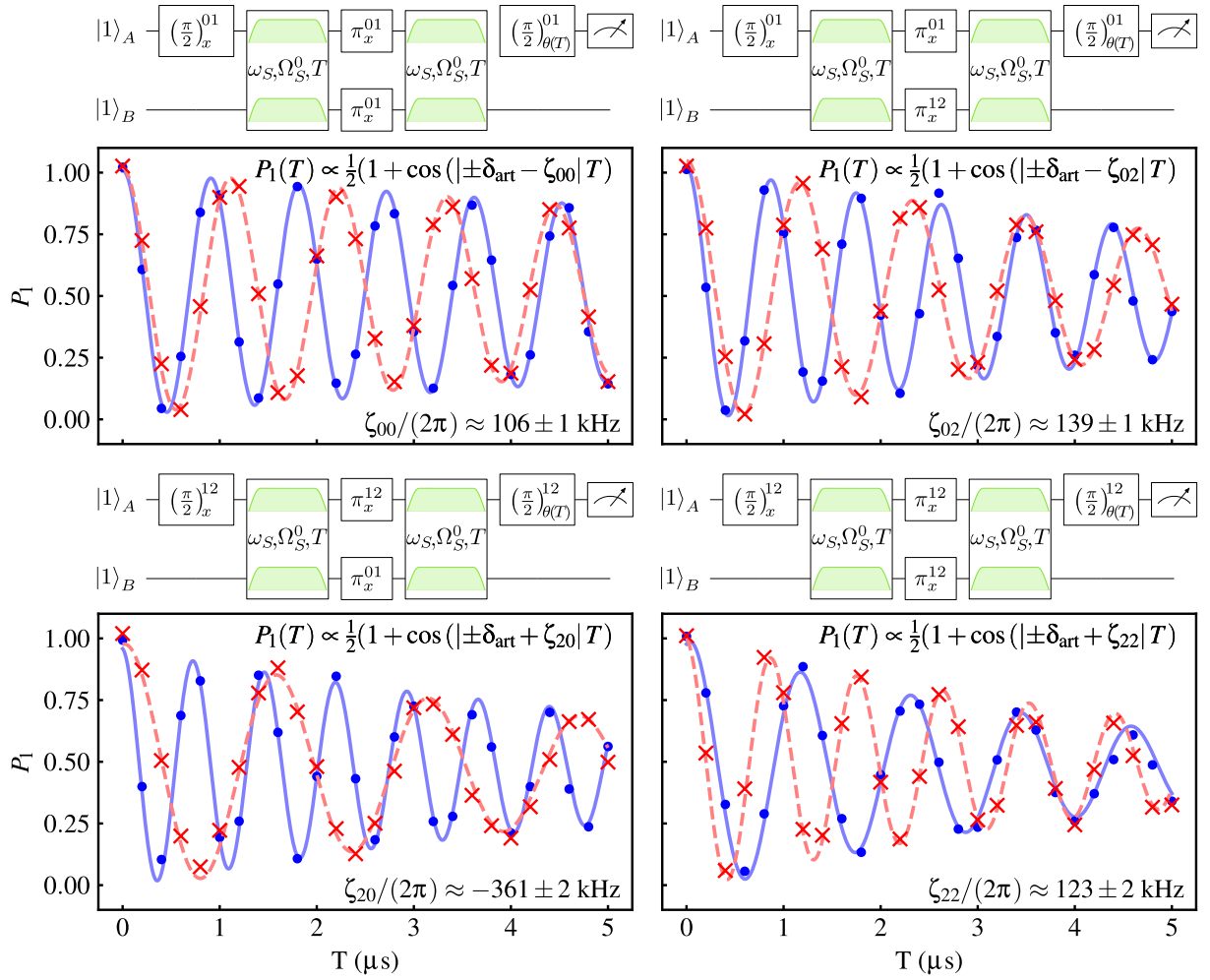


FIG. 9: JAZZ sequence circuit diagrams and measurement results to estimate Stark-driven $\tilde{\zeta}_{ij}$ entangling rates. Each circuit is run twice, with $\theta(T) = \pm\delta_{\text{art}}T$ (+: blue circles, solid line fit; -: red crosses, dashed line fit), and the signed values of ζ_{ij} are extracted from exponentially decaying cosine fits of the two measurements. The artificial detuning was $\delta_{\text{art}}/2\pi = 1$ MHz for all measurements. These measurements were taken with a calibrated Stark drive, yielding $\tilde{z}_{22} = \frac{1}{4}(\tilde{\zeta}_{00} + \tilde{\zeta}_{02} + \tilde{\zeta}_{20} + \tilde{\zeta}_{22}) \approx -2$ kHz.

Appendix E: Analog-Digital Simulation Coherence Times and Heuristic Average Decay Model

The coherence times and other relevant parameters of the two transmons used in the analog-digital experiment are given in Table I.

In the single qutrit experiment, we assume Markovian noise processes and model decoherence with the Lindblad master equation [115]

$$\begin{aligned} \dot{\rho} &= -i[H, \rho] + \sum_{\alpha} \Gamma_{\alpha} \left(L_{\alpha} \rho L_{\alpha}^{\dagger} - \frac{1}{2} L_{\alpha}^{\dagger} L_{\alpha} \rho - \frac{1}{2} \rho L_{\alpha}^{\dagger} L_{\alpha} \right) \\ &\equiv \mathcal{L}(\rho), \end{aligned} \quad (\text{E1})$$

where the Hamiltonian is taken to be the single-qutrit Hamiltonian in Eq. (7), $\mathcal{L}(\cdot)$ is the Liouville superoperator, and the transmon's Lindblad jump opera-

	QA	QB
$\omega_{01}/2\pi$ (GHz)	5.4146	5.2484
$\omega_{12}/2\pi$ (GHz)	5.1687	5.0075
$\omega_{23}/2\pi$ (GHz)	4.918	4.758
T_1^{01} (μs)	30(3)	26(7)
T_{2R}^{01} (μs)	48(8)	36(14)
T_1^{12} (μs)	15(4)	17(5)
T_{2R}^{12} (μs)	20(10)	24(9)
ω_S (GHz)	5.08	5.08
Ω_S^0 (MHz)	7.1	7.1
J (MHz)	2	

TABLE I: Relevant parameters of the two transmons in the Rochester-based device used in the analog-digital experiment.

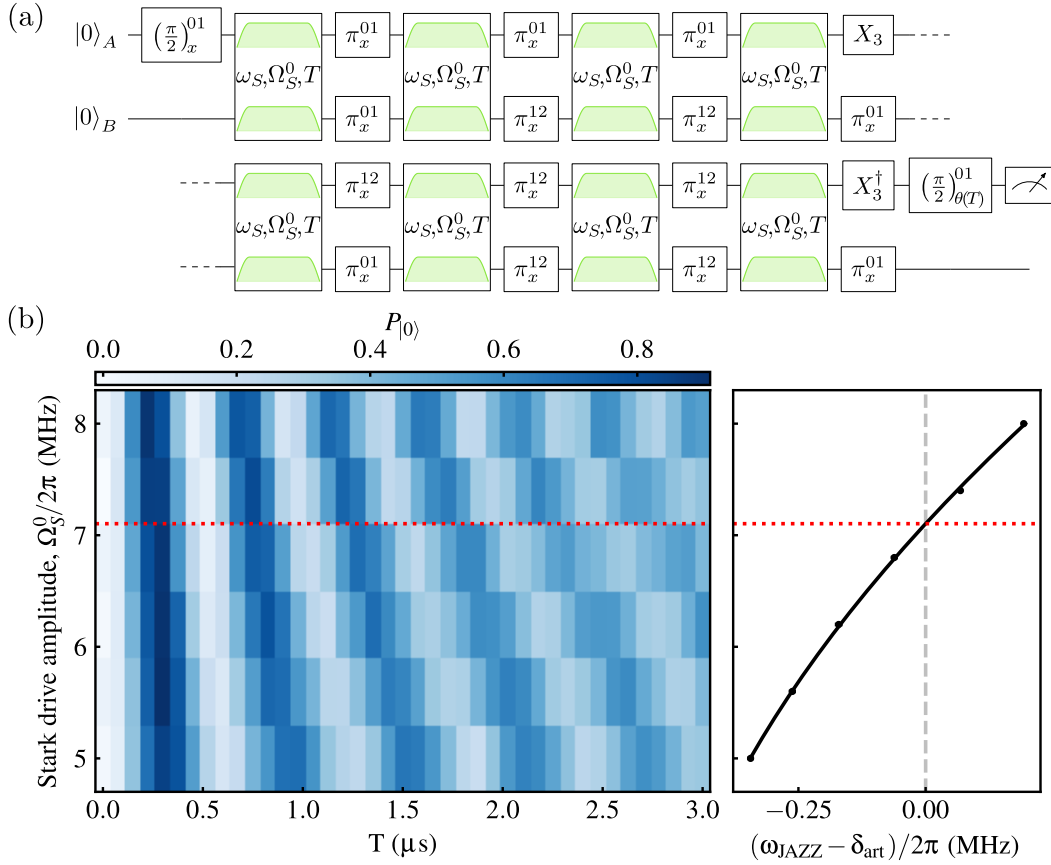


FIG. 10: Circuit diagram and calibration measurement for the Stark drive amplitude. (a) “Total JAZZ” sequence, designed to produce oscillations in T at a frequency corresponding to $\zeta_{00} + \zeta_{02} + \zeta_{20} + \zeta_{22} = 4z_{22}$. The circuit is split into two lines for clarity. The “shift” gate $X_d = \sum_n^{d-1} |n+1 \pmod d\rangle \langle n|$ (see, e.g. [83, 114]) may be performed on a qutrit with two π pulses: $X_3 = \pi_x^{01} \pi_x^{12}$. (b) Stark drive amplitude calibration measurement with the “Total JAZZ” sequence. Given a particular ω_S , we perform the circuit in (a) for varying Stark drive amplitudes Ω_S^0 and varying drive durations T . At each value of Ω_S^0 , the Ramsey oscillations in the left panel are fit with an exponentially decaying cosine function, and the resulting oscillation frequencies, with the artificial detuning of $\delta_{\text{art}} = 3$ MHz subtracted, are shown in the right panel. The frequencies are then fit with a quadratic as a function of Ω_S^0 , and the zero crossing point is solved for analytically, providing the calibrated Stark drive amplitude.

tors [68, 116]

$$\begin{aligned} L_{10} &= |0\rangle\langle 1|, & L_{11} &= |1\rangle\langle 1|, \\ L_{21} &= |1\rangle\langle 2|, & L_{22} &= |2\rangle\langle 2|, \end{aligned} \quad (\text{E2})$$

describe the decay of the excited states (L_{10}, L_{21}) and pure dephasing (L_{11}, L_{22}). The corresponding rates Γ_{ij} are calculated from the coherence times reported in Table I as

$$\begin{aligned} \Gamma_{10} &= (T_1^{01})^{-1}, & \Gamma_{11} &= (T_2^{01})^{-1} - \frac{1}{2}(T_1^{01})^{-1}, \\ \Gamma_{21} &= (T_1^{12})^{-1}, & \Gamma_{22} &= (T_2^{12})^{-1} - \frac{1}{2}(T_1^{12})^{-1}. \end{aligned} \quad (\text{E3})$$

In the two-qutrit experiment, we alternate long periods of evolution ($T_E = 800$ ns) with relatively brief unitary operations ($T_g = 60$ ns) to approximate the time-independent Hamiltonian H_{AHM} . To account for decoherence with a time-independent master equation model,

we assume a modified set of Lindblad jump operators, which we justify here.

During each evolution period between swaps, the evolution may be formally written $\rho(t) = e^{\mathcal{L}t}(\rho(0))$ [117]. By preceding the evolution period with the application of a unitary U and following it with the inverse U^\dagger —both assumed to be instantaneous—we may write the new evolution as

$$\tilde{\rho}(t) = U^\dagger(e^{\mathcal{L}t}(U(\rho(0)))) \quad (\text{E4})$$

where we define the superoperator $\mathcal{U}(\cdot) = U \cdot U^\dagger$. By expanding the exponential operator, we may see that $\mathcal{U}, \mathcal{U}^\dagger$ may be absorbed into the exponential:

$$\mathcal{U}^\dagger(e^{\mathcal{L}t}(U(\cdot))) = e^{\mathcal{U}^\dagger \mathcal{L} \mathcal{U} t}(\cdot), \quad (\text{E5})$$

leading to a new Liouvillian:

$$\begin{aligned}
(\mathcal{U}^\dagger \mathcal{L} \mathcal{U})(\rho) &= -iU^\dagger[H, U\rho U^\dagger]U + \sum_\alpha \Gamma_\alpha U^\dagger \left(L_\alpha U\rho U^\dagger L_\alpha^\dagger - \frac{1}{2}L_\alpha^\dagger L_\alpha U\rho U^\dagger - \frac{1}{2}U\rho U^\dagger L_\alpha^\dagger L_\alpha \right) U \\
&= -i[\tilde{H}, \rho] + \sum_\alpha \Gamma_\alpha \left(\tilde{L}_\alpha \rho \tilde{L}_\alpha^\dagger - \frac{1}{2}\tilde{L}_\alpha^\dagger \tilde{L}_\alpha \rho - \frac{1}{2}\rho \tilde{L}_\alpha^\dagger \tilde{L}_\alpha \right) \\
&\equiv \tilde{\mathcal{L}}(\rho),
\end{aligned} \tag{E6}$$

where we have defined the toggling frame Hamiltonian $\tilde{H} = U^\dagger H U$ and jump operators $\tilde{L}_\alpha = U^\dagger L_\alpha U$.

Next, assuming the evolution time T_E is short compared to the timescales of the evolution—set by H and the Γ_α —we may approximate the exponential evolution under the Lindblad equation to first order in T_E as,

$$\rho(T_E) = e^{\mathcal{L}T_E}(\rho(0)) \approx (1 + \mathcal{L}T_E)(\rho(0)). \tag{E7}$$

Then using $\rho(T_E)$ as the initial state for evolution under $\tilde{\mathcal{L}}$, we find, again to first order,

$$\begin{aligned}
\rho(2T_E) &= e^{\tilde{\mathcal{L}}T_E}(\rho(T_E)) \approx (1 + \tilde{\mathcal{L}}T_E)(1 + \mathcal{L}T_E)(\rho(0)) \\
&= (1 + \tilde{\mathcal{L}}T_E + \mathcal{L}T_E + \tilde{\mathcal{L}}\mathcal{L}T_E^2)(\rho(0)) \\
&\approx (1 + \tilde{\mathcal{L}}T_E + \mathcal{L}T_E)(\rho(0)) \\
&\approx e^{(\tilde{\mathcal{L}}+\mathcal{L})T_E}(\rho(0)).
\end{aligned} \tag{E8}$$

The effective average Liouville operator for the evolution over two periods is then

$$\begin{aligned}
\frac{1}{2}(\tilde{\mathcal{L}} + \mathcal{L})(\rho) &= -i\frac{1}{2}[H + \tilde{H}, \rho] \\
&+ \frac{1}{2} \sum_\alpha \Gamma_\alpha \left(L_\alpha \rho L_\alpha^\dagger - \frac{1}{2}L_\alpha^\dagger L_\alpha \rho - \frac{1}{2}\rho L_\alpha^\dagger L_\alpha \right) \\
&+ \frac{1}{2} \sum_\alpha \Gamma_\alpha \left(\tilde{L}_\alpha \rho \tilde{L}_\alpha^\dagger - \frac{1}{2}\tilde{L}_\alpha^\dagger \tilde{L}_\alpha \rho - \frac{1}{2}\rho \tilde{L}_\alpha^\dagger \tilde{L}_\alpha \right) \\
&\approx \mathcal{L}_{\text{eff}}(\rho).
\end{aligned} \tag{E9}$$

The Hamiltonian part of the operator is the first order average Hamiltonian as discussed in the main text, and the set of jump operators L_α are defined for each qutrit as in Eq. (E2).

Because the Lindblad equation assumes Markovianity, we expect this average-Lindblad model to miss potential dynamical decoupling effects due to the periodic pulses. However, the level of agreement found between numerical evolution of the model and the data indicates that such effects do not significantly contribute to the evolution here.

Appendix F: Error Analysis in Analog-Digital Simulation

In this appendix, we apply average Hamiltonian theory (AHT) to analyze coherent errors in the two-qutrit analog-digital protocol. We address two distinct sources

of error: (1) errors arising from the failure of the Stark-driven Hamiltonian to commute with itself over the course of a single pulse, and (2) errors arising from higher-order terms in the dynamical decoupling sequence.

To analyze the errors within the pulse originating from pulse shaping, we start with the system Hamiltonian in the drive frame from Eq. (17):

$$\begin{aligned}
H_{\text{sys}}(t) &= A(t) \left(\Delta_0 L_z^2 + \frac{\Omega_0}{\sqrt{2}} L_x \right) \otimes I \\
&+ I \otimes A(t) \left(\Delta_0 L_z^2 + \frac{\Omega_0}{\sqrt{2}} L_x \right) \\
&+ A(t) \sum_{ij=1}^2 \delta z_{ij} L_z^i \otimes L_z^j + \sum_{ij=1}^2 z_{ij}^0 L_z^i \otimes L_z^j,
\end{aligned} \tag{F1}$$

where we define $A(t)\delta z_{ij} = \tilde{z}_{ij}(t) - z_{ij}^0$ as the part of the entangling Hamiltonian that depends on the Stark drives (see Appendix C). Throughout this section, superscripts on the L_α operators will indicate powers, with the site index indicated by their position relative to the \otimes symbol. Because the time-dependent parts of the Hamiltonian are all constructed to vary with the same envelope $A(t)$ (see the main text), we may write

$$\begin{aligned}
H_{\text{sys}}(t) &= A(t)M_1 + \sum_{ij=1}^2 z_{ij}^0 L_z^i \otimes L_z^j \\
&\equiv H(t) + H_0,
\end{aligned} \tag{F2}$$

where M_1 contains the structure of the time-dependent part of Eq. (F1). We are then interested in taking the Magnus expansion of this Hamiltonian to third order to get the effective time-independent Hamiltonian that describes the evolution over a single evolution period. See Eqs. (A4)–(A6) in Appendix A for definitions of the first several terms in the Magnus expansion. The first order term is given in Eq. (18), and the higher order terms produce coherent errors.

We first compute the commutators for the integrands of the second and third-order terms. Using the fact that we wrote our Hamiltonian as a time-dependent and a time-independent part, we can simplify our calculation of the commutators with $[H_0, H_0] = 0$ and $[H(t), H(t')] = A(t)A(t')[M_1, M_1] = 0$, thus the only contributions will come from the commutator of the time-independent and time-dependent parts and their nested

commutators. With that we can write:

$$\begin{aligned} [H_{\text{sys}}(t), H_{\text{sys}}(t')] &= [H(t), H_0] - [H(t'), H_0] \\ &\equiv \mathcal{C}_{10}(t) - \mathcal{C}_{10}(t'), \end{aligned}$$

where we define $\mathcal{C}_{10}(t)$ for later convenience. The subscript refers to the terms in the (nested) commutator sequence, where we use 1 to denote $H(t)$ and a 0 denotes H_0 . Similarly, for the third order commutators,

$$\begin{aligned} [H_{\text{sys}}(t), [H_{\text{sys}}(t'), H_{\text{sys}}(t'')]] &= [H_{\text{sys}}(t), \mathcal{C}_{10}(t')] \\ &\quad - [H_{\text{sys}}(t), \mathcal{C}_{10}(t'')] \\ &= [H(t), \mathcal{C}_{10}(t')] - [H(t), \mathcal{C}_{10}(t'')] \\ &+ [H_0, \mathcal{C}_{10}(t')] - [H_0, \mathcal{C}_{10}(t'')] \\ &\equiv \mathcal{C}_{110}(t, t') - \mathcal{C}_{110}(t, t'') + \mathcal{C}_{010}(t') - \mathcal{C}_{010}(t'') \\ \\ [H_{\text{sys}}(t), H_{\text{sys}}(t'), H_{\text{sys}}(t'')] &= -[H_{\text{sys}}(t''), [H_{\text{sys}}(t), H_{\text{sys}}(t')]] \\ &\equiv \mathcal{C}_{110}(t'', t') - \mathcal{C}_{110}(t'', t) + \mathcal{C}_{010}(t') - \mathcal{C}_{010}(t). \end{aligned}$$

Finally, we need to evaluate the forms of the operators $\mathcal{C}_{10}(t)$, $\mathcal{C}_{110}(t, t')$, and $\mathcal{C}_{010}(t)$ before computing the integrals. The second-order commutator can be written,

$$\begin{aligned} \mathcal{C}_{10}(t) &= A(t) \frac{\Omega}{\sqrt{2}} \sum_{ij} z_{ij}^0 \left([L_x, L_z^i] \otimes L_z^j + L_z^i \otimes [L_x, L_z^j] \right) \\ &\equiv A(t) M_2. \end{aligned}$$

The third-order commutators are,

$$\begin{aligned} \mathcal{C}_{010}(t) &= -A(t) \frac{\Omega_0}{\sqrt{2}} \sum_{ij} z_{ij}^0 \sum_{kl} z_{kl}^0 \left([L_z^i, [L_x, L_z^k]] \otimes L_z^{l+j} \right. \\ &\quad \left. + L_z^{k+i} \otimes [L_z^j, [L_x, L_z^l]] \right) \\ &\equiv A(t) M_{3,1}, \end{aligned}$$

$$\begin{aligned} \mathcal{C}_{110}(t, t') &= A(t) A(t') \frac{\Omega_0}{\sqrt{2}} \sum_{ij} z_{ij}^0 \left\{ \frac{\Omega_0}{\sqrt{2}} \left([L_x, [L_x, L_z^i]] \otimes L_z^j + L_z^i \otimes [L_x, [L_x, L_z^j]] \right) \right. \\ &\quad + \Delta_0 \left([L_z^2, [L_x, L_z^i]] \otimes L_z^j + L_z^i \otimes [L_z^2, [L_x, L_z^j]] \right) \\ &\quad + \sum_{kl} \delta z_{kl} \left([L_z^k, [L_x, L_z^i]] \otimes L_z^{j+l} + L_z^{i+k} \otimes [L_z^l, [L_x, L_z^j]] \right) \\ &\quad \left. + 2 \frac{\Omega_0}{\sqrt{2}} [L_x, L_z^i] \otimes [L_x, L_z^j] \right\} \\ &\equiv A(t) A(t') M_{3,2}. \end{aligned}$$

With that in hand, the orders of Magnus expansion can be written as

$$\begin{aligned} \bar{H}^{(1)} &= \frac{B(T)}{T} \left[\left(\Delta_0 L_z^2 + \frac{\Omega_0}{\sqrt{2}} L_x \right) \otimes I \right. \\ &\quad \left. + I \otimes \left(\Delta_0 L_z^2 + \frac{\Omega_0}{\sqrt{2}} L_x \right) + \sum_{ij} \delta z_{ij} L_z^i \otimes L_z^j \right] \quad (\text{F3}) \\ &\quad + \sum_{ij} z_{ij}^0 L_z^i \otimes L_z^j \\ &= M_1 + H_0, \end{aligned}$$

where $B(t) \equiv \int_0^t A(t') dt'$ and $B(T) = T$ by definition.

The second-order term becomes:

$$\begin{aligned} \bar{H}^{(2)} &= \frac{M_2}{2iT} \int_0^T \int_0^t A(t) - A(t') dt' dt \\ &= \frac{M_2}{2iT} \int_0^T (tA(t) - B(t)) dt. \end{aligned} \quad (\text{F4})$$

For any $A(t)$ symmetric around $t = T/2$, this integral evaluates to $\bar{H}^{(2)} = 0$. And finally, the third-order term

can be written as

$$\begin{aligned}
\bar{H}^{(3)} &= \frac{-1}{6T} \int_0^T \int_0^t \int_0^{t'} \left(\mathcal{C}_{110}(t, t') + \mathcal{C}_{110}(t'', t') \right. \\
&\quad \left. + \mathcal{C}_{010}(t) - 2\mathcal{C}_{010}(t') + \mathcal{C}_{010}(t'') \right) dt'' dt' dt \\
&= \frac{-1}{6T} \int_0^T \int_0^t \int_0^{t'} \left(A(t)A(t') + A(t')A(t'') \right) M_{3,2} \\
&\quad + \left(A(t) - 2A(t') + A(t'') \right) M_{3,1} dt'' dt' dt \\
&= \alpha(r, T)M_{3,2} + \beta(r, T)M_{3,1},
\end{aligned} \tag{F5}$$

where $\alpha(r, T)$ and $\beta(r, T)$ are functions of the ramp fraction and the evolution time only and, for the envelope defined in Eq. (B7), are given by

$$\alpha(r, T) = T^2 \frac{(33 - 6\pi^2)r^3 + 3r^2(\pi^2 - 8) + 6\pi^2r - 4\pi^2}{72\pi^2(1-r)^2}$$

$$\beta(r, T) = \frac{rT^2}{12} \left[1 + \left(\frac{12}{\pi^2} - 2 \right) r \right].$$

Taking the fact that all parameters in the Hamiltonian for the analog-digital two-qutrit experiment were on the order of 100 kHz, and using the evolution time $T = T_E = 800$ ns, we may estimate the total contribution of $\bar{H}^{(3)}$ to be $|\bar{H}^{(3)}| < 0.1$ kHz.

We now compute the errors due to higher-order terms in the dynamical decoupling sequence. We assume that the sequence alternates between time-independent Hamiltonians \bar{H}_{sys} and $\tilde{H}_{\text{sys}} = U_{02}^\dagger \bar{H}_{\text{sys}} U_{02}$, where $U_{02} = \pi_{02} \otimes \pi_{02}$ is considered to be instantaneous and perfect. Considering the order of magnitude of the error terms found above, we will simplify the calculation with the assumption that \bar{H}_{sys} is well approximated by the first order term Eq. (F3). We can then use the discrete effective average Hamiltonian $\bar{H}_{\text{disc}} \approx \bar{H}_{\text{disc}}^{(1)} + \bar{H}_{\text{disc}}^{(2)}$ with Hamiltonian terms defined in Eqs. (A7)–(A8).

The first order term,

$$\begin{aligned}
\bar{H}_{\text{disc}}^{(1)} &= \left(\Delta_0 L_z + \frac{\Omega_0}{\sqrt{2}} L_x \right) \otimes I + I \otimes \left(\Delta_0 L_z + \frac{\Omega_0}{\sqrt{2}} L_x \right) \\
&\quad + \tilde{z}_{11} L_z \otimes L_z + \tilde{z}_{22} L_z^2 \otimes L_z^2,
\end{aligned} \tag{F6}$$

produces the target Hamiltonian H_{AHM} when we account for the calibration $\tilde{z}_{22} \approx 0$. To compute the second order term, we first observe that the only terms affected by conjugating with U_{02} are the odd-parity interaction terms $L_z L_z^2$ and $L_z^2 L_z$, and second, we observe that the only terms that do not commute with those are the on-site drives L_x . This simplifies the calculation of the commutator:

$$\begin{aligned}
\bar{H}_{\text{disc}}^{(2)} &= -\frac{\Omega_0 T}{2} \left\{ \tilde{z}_{12} (L_y \otimes L_z^2 + L_z \otimes [L_x, L_z^2]) \right. \\
&\quad \left. + \tilde{z}_{21} ([L_x, L_z^2] \otimes L_z + L_z^2 \otimes L_y) \right\}
\end{aligned} \tag{F7}$$

The order of magnitude of these errors given the parameters of the two-qutrit experiment is $|\bar{H}_{\text{disc}}^{(2)}| \sim 20$ kHz, making this the dominant coherent error term of those examined.

Remaining error sources we have not analyzed rigorously include the finite duration and imperfect fidelity of the U_{02} pulses and the validity of the adiabatic condition during the Stark drive ramps.

Appendix G: Device-specific details of the digital quantum simulator

In this appendix, we provide the matrix representation of the quantum operations that are the building blocks of our theory and provide the basis gate-set that are available in the AQT device where we performed our digital quantum simulation.

Single qutrit operations in the Abelian Higgs model are realized by the following quantum operations

$$M_z = \text{diag}(\exp(i\theta), 1, \exp(i\theta)) \tag{G1}$$

and,

$$M_x = \begin{pmatrix} \cos^2\left(\frac{\phi}{2\sqrt{2}}\right) & \frac{-i}{\sqrt{2}} \sin\left(\frac{\phi}{\sqrt{2}}\right) & -\sin^2\left(\frac{\phi}{2\sqrt{2}}\right) \\ \frac{-i}{\sqrt{2}} \sin\left(\frac{\phi}{\sqrt{2}}\right) & \cos\left(\frac{\phi}{\sqrt{2}}\right) & \frac{-i}{\sqrt{2}} \sin\left(\frac{\phi}{\sqrt{2}}\right) \\ -\sin^2\left(\frac{\phi}{2\sqrt{2}}\right) & \frac{-i}{\sqrt{2}} \sin\left(\frac{\phi}{\sqrt{2}}\right) & \cos^2\left(\frac{\phi}{2\sqrt{2}}\right) \end{pmatrix}; \tag{G2}$$

whereas nearest-neighbor spin-1 Ising interaction terms are the entangling operations

$$M_{zz} = \text{diag}(e^{i\gamma}, 1, e^{-i\gamma}, 1, 1, e^{-i\gamma}, 1, e^{i\gamma}). \tag{G3}$$

We discussed the unitary decomposition of the above quantum operations into elementary gates in the main text. For the decomposition, we used the Gell-Mann matrices which are a standard choice of generators for $\text{SU}(3)$:

$$\begin{aligned} \lambda_1 \equiv \sigma_x^{01} &= \begin{pmatrix} 0 & 1 & 0 \\ 1 & 0 & 0 \\ 0 & 0 & 0 \end{pmatrix}, & \lambda_2 \equiv \sigma_y^{01} &= \begin{pmatrix} 0 & -i & 0 \\ i & 0 & 0 \\ 0 & 0 & 0 \end{pmatrix}, & \lambda_3 \equiv \sigma_z^{01} &= \begin{pmatrix} 1 & 0 & 0 \\ 0 & -1 & 0 \\ 0 & 0 & 0 \end{pmatrix}, \\ \lambda_4 \equiv \sigma_x^{02} &= \begin{pmatrix} 0 & 0 & 1 \\ 0 & 0 & 0 \\ 1 & 0 & 0 \end{pmatrix}, & \lambda_5 \equiv \sigma_y^{02} &= \begin{pmatrix} 0 & 0 & -i \\ 0 & 0 & 0 \\ i & 0 & 0 \end{pmatrix}, & \lambda_6 \equiv \sigma_x^{12} &= \begin{pmatrix} 0 & 0 & 0 \\ 0 & 0 & 1 \\ 0 & 1 & 0 \end{pmatrix}, \\ \lambda_7 \equiv \sigma_y^{12} &= \begin{pmatrix} 0 & 0 & 0 \\ 0 & 0 & -i \\ 0 & i & 0 \end{pmatrix}, & \lambda_8 &= \frac{1}{\sqrt{3}} \begin{pmatrix} 1 & 0 & 0 \\ 0 & 1 & 0 \\ 0 & 0 & -2 \end{pmatrix}. \end{aligned}$$

These are Hermitian matrices with zero trace, and orthogonal under trace. The Gell-Mann matrices (λ_i) constitute a viable set of generators of SU(3), providing universal control for a single qutrit. For convenience, we define an additional Hermitian operator, $\sigma_z^{12} \equiv -\frac{1}{2}\lambda_3 - \frac{\sqrt{3}}{2}\lambda_8$, which is not orthogonal to σ_z^{01} , but which corresponds to qubit-like rotations about the z axis in the $\{|1\rangle, |2\rangle\}$ subspace and is naturally implemented by shifting the phase of the drive on the $|1\rangle \leftrightarrow |2\rangle$ transition.

We can use either the two-qudit controlled-SUM or controlled-Z gates for realizing the entangling operations, given by [83]

$$U_{\text{CSUM}} = \sum_{n=0}^{d-1} |n\rangle\langle n| \otimes X_d^n \quad (\text{G4})$$

$$= \left(I \otimes H_d^\dagger \right) U_{\text{CZ}} \left(I \otimes H_d \right) \quad (\text{G5})$$

$$U_{\text{CZ}} = \sum_{n=0}^{d-1} |n\rangle\langle n| \otimes Z_d^n, \quad (\text{G6})$$

where,

$$X_d = \sum_{n=0}^{d-1} |n+1 \pmod{d}\rangle\langle n|, \quad (\text{G7})$$

$$Z_d = \sum_{n=0}^{d-1} \exp\left(i\frac{2\pi n}{d}\right) |n\rangle\langle n|, \quad (\text{G8})$$

$$H_d = \frac{1}{\sqrt{d}} \sum_{n,m=0}^{d-1} \exp\left(i\frac{2\pi}{d}nm\right) |n\rangle\langle m|. \quad (\text{G9})$$

The CSUM and CZ gates are the qudit generalization of the qubit CNOT and controlled-Z gate.

Our native gate for two-qutrit operations is the qutrit-CZ gate defined by the unitary

$$U_{\text{CZ}} = \sum_{i,j=0}^2 \omega^{ij} |ij\rangle\langle ij| \quad (\text{G10})$$

where $\omega = e^{i2\pi/3}$ is the third root of unity. To realize the gate on our device, we employ simultaneous off-resonant

microwave drives to realize a tunable cross-Kerr interaction in our coupled qutrit system and employ dynamical decoupling to engineer the specific target unitary of U_{CZ} . More information on how the gate is performed can be found in Ref. [78]. We use the same principle in without the requirement that the final unitary is U_{CZ} to engineer the interaction Hamiltonian for the analog-digital hybrid simulation.

	QA	QB
Qubit freq. (GHz)	5.374	5.443
Anharm. (MHz)	-274	-271
T_1^{01} (μs)	60(13)	47(14)
T_1^{12} (μs)	36(4)	34(5)
T_{2e}^{01} (μs)	69(7)	61(14)
T_{2e}^{12} (μs)	32(5)	32(6)
$\tau_{1Q,X90}$ (ns)	30	30
$\tau_{1Q,SU(3)}$ (ns)	180	180
τ_{2Q} (ns)	612	

TABLE II: Device parameters for the Berkeley based qutrit processor used in the digital quantum simulations. Decoherence times (T), various native and composite gate times (τ) are listed along with qubit frequencies and anharmonicities used in the digital experiments.

Appendix H: Error mitigation in qutrit-based simulation

In this appendix section, we review the error mitigation scheme developed in earlier studies [63, 118] which proved instrumental for improving the time scale over which we could observe dynamics. Our error strategy is two-fold: firstly we apply randomized compilation to tailor our error model to be stochastic Pauli noise (approximately depolarizing), and secondly we numerically purify our expectation values using noise measured by cycle benchmarking. In addition, readout error mitigation is applied to reduce remove state preparation and measurement errors.

We can construct a stochastic channel efficiently by

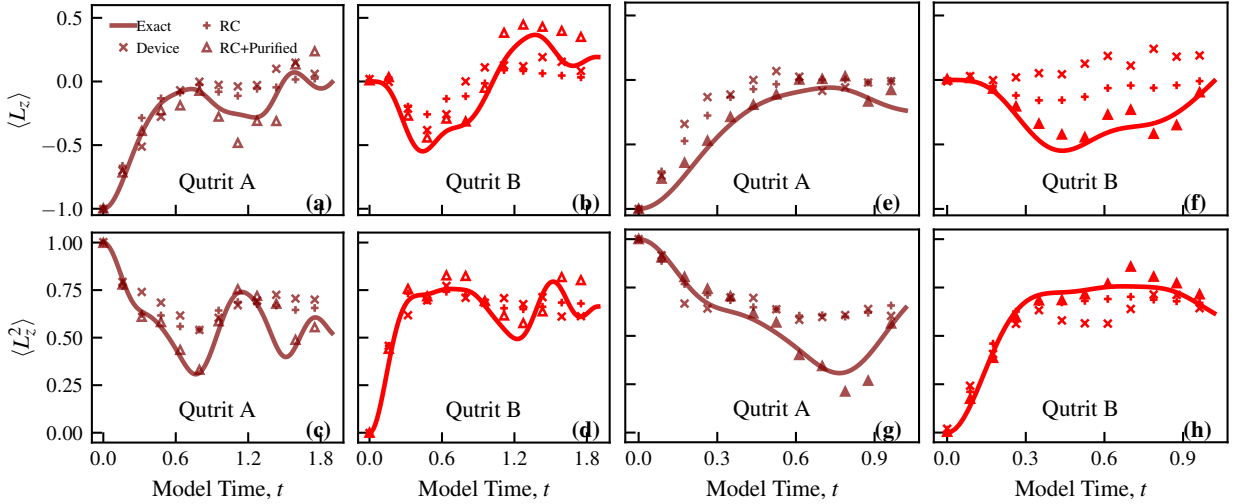


FIG. 11: Impact of error mitigation scheme is investigated in two experiments with different Trotter steps. A larger Trotter step ($\delta t = 1.0$) allows us to observe real-time dynamics longer times (a-d), whereas a smaller Trotter step ($\delta t = 0.55$) reduces Trotter error but limits the accessible timescale (e-h). In both experiments, we find error mitigation schemes to be effective in improving fidelity of our quantum operations on average. For both experiments, we present here raw hardware data (Device), error-mitigated device data with randomized compilation (RC), data with randomized compilation and numerical purification (RC+purified), and compare them with exact diagonalization (Exact) for qutrit A (Maroon) and qutrit B (Red). Expectation values are computed for an initial state [21]. We note that statistical errors in our experiments are insignificant compared to other sources of error in the experiment. Statistical error scales as the inverse of the square root of the number of shots and thus statistical errors in our experiment are of the order $\sim \frac{1}{\sqrt{1024 \times 30}} \sim 0.006$.

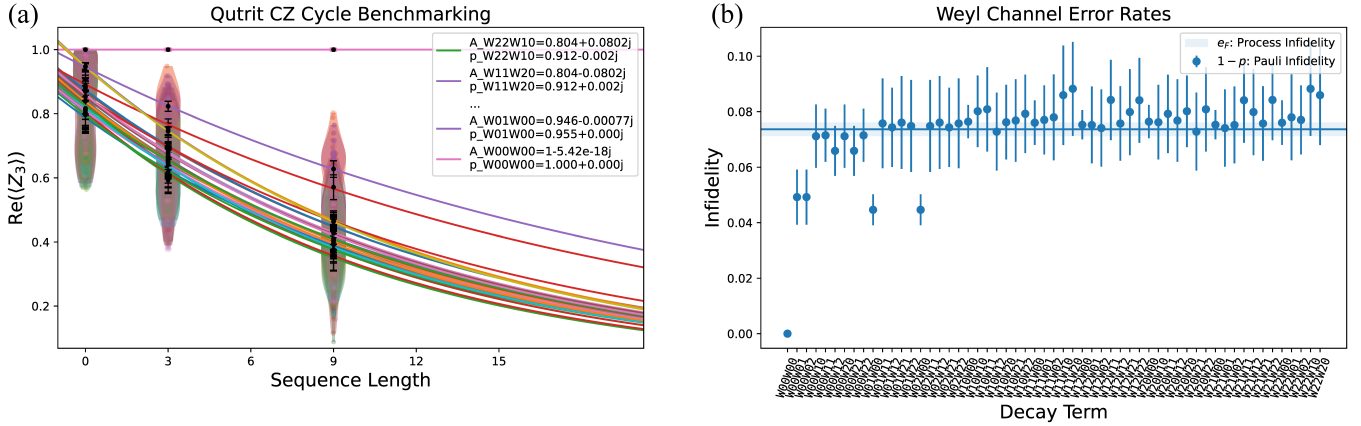


FIG. 12: Cycle Benchmarking results for our two-qutrit CZ gate employed as the native entangling gate in the digital quantum simulations of the Abelian Higgs model. (a) The violin plots of individual Weyl decay exponentials and their associated uncertainty. Both the SPAM parameter (A) and the decay term (p) are fit for each prepared Weyl eigenstate. (b) The infidelity and uncertainty associated with each decay term extracted from fitting the Weyl eigenstate decays from our CB circuits.

sampling from a unitary-1 design [119]. We choose Weyl (qudit Pauli) operators as the unitary-1 design to perform twirling for randomized compilation. Weyl operators form a group over $SU(d)$ with group elements defined as $W_{k,l} = \omega^{-kl/2} Z^k X^l$ where X and Z gates are defined by their action on the occupation basis as $|m\rangle = \{|0\rangle, |1\rangle, |2\rangle\}$ such that $X|m\rangle = |m \oplus 1\rangle$ and

$Z|m\rangle = \omega^m |m\rangle$, with $\omega = \exp(i\frac{2\pi}{3})$. It is worth mentioning that using higher dimensional qudits as our quantum computing unit does not increase the overhead (number of twirling circuits) required to achieve equal suppression of coherent noise with randomized compilation [63]. To achieve effective coherent error suppression, we perform 30 equivalent twirled circuits for each initial circuit. In

principle, employing randomized compiling does not incur a runtime overhead as the number of desired shots per circuit can be evenly divided evenly over the twirled circuits.

Our strategy after performing randomized compiling to mitigate coherent noise is to learn and numerically purify the incoherent noise in our system. Formally, incoherent noise can be defined in terms of error rates associated with Weyl channels. A Weyl channel can be expressed as

$$\begin{aligned} \mathcal{E}(\rho) &= \sum_{p,q=0}^2 w_{p,q} W_{p,q} \rho W_{p,q}^\dagger \\ &= w_{0,0} \rho + \sum_{p,q,p+q \neq 0} w_{p,q} W_{p,q} \rho W_{p,q}^\dagger \end{aligned} \quad (\text{H1})$$

We efficiently learn the error rate $w_{p,q}$ of the Weyl channels $W_{p,q}$ using cycle benchmarking [90]. Cycle benchmarking is performed by executing the following steps

- Prepare eigenstates of a randomly chosen Weyl channel.
- Select a cycle (e.g. our native two-qudit gate) and repeat it N -times. In between each cycle perform Weyl twirling to turn the channel into a stochastic one.
- Measure the expectation value of the same Weyl operator after N times.

Repeating the steps for several layers (N) and initial choice of Weyl eigenstates, the decay rate of each associated channel can be measured by fitting its corresponding error curve. The cycle benchmarking results of our two-qutrit CZ gate can be found in Fig. 12.

We can estimate an effective depolarizing noise parameter from the average of our Weyl decay terms measured by cycle benchmarking. We note this simplified depolarizing noise model for our system takes the form,

$$\epsilon(\rho) = \lambda \rho + (1 - \lambda) \frac{I_3}{3^N} \quad (\text{H2})$$

As can be observed in Fig. 12, the fairly even distribution of Weyl decay terms makes this a reasonable approximation. To mitigate our incoherent noise, the estimated depolarization strength is used to rescale the Z expectation values measured from our twirled circuits, providing a more accurate estimate of the observables. For a detailed discussion on Weyl twirling and cycle benchmarking, readers are advised to consult [63, 120].

The impact of applying these mitigation schemes proved instrumental in recovering useful dynamics. Fig 11 demonstrates how randomized compilation and purification improved the estimate of the field operator estimates $\langle L_z \rangle$ and $\langle L_z^2 \rangle$. It is clear that twirling itself is not always sufficient to recover low-error estimates as decoherence dominates beyond very shallow circuit depths. A combination of mitigation schemes namely, randomized compilation and purification, proved essential in reducing coherent and incoherent errors.

Appendix I: Resource estimation and comparison with qubit-based simulation

We provide arguments in this appendix on the advantages of qutrit-based time-evolution of spin-1 quantum system over qubit-based formulations.

To map an N -qutrit three level system in a qubit platform, we require $N \log_2 3$ qubit. A possible mapping of the spin-1 eigenstates to the occupation basis using standard binary encoding is

$$\begin{aligned} |m = 1\rangle &\rightarrow |n = 00\rangle, & |m = 0\rangle &\rightarrow |n = 01\rangle, \\ |m = -1\rangle &\rightarrow |n = 10\rangle. \end{aligned} \quad (\text{I1})$$

With this encoding, different quantum operations required to implement the propagator of the AHM is shown in Fig. 13. We did not investigate other encoding schemes for this study. It is worth mentioning that there is no unique encoding scheme that is advantageous for all sorts of different quantum operations [121]. We performed both analytic and transpiler-based decomposition for each quantum operation for the standard binary encoding. We find the decomposition obtained from the Bqskit transpiler [122] optimal with fewer entangling operations for all the cases. Two-qubit unitary synthesis of our single qutrit operation M_x^i require two CNOT gates whereas 4-qubit decomposition of the original entangling operation M_{zz}^i require 12-CNOT gates if we consider all-to-all topology of qubits in the hardware. For the restricted topology, for example with IBM's Heron r3 processor, we require 30 CNOT gates. This clearly demonstrates that for a matured technology with comparable decoherence times, qutrit simulation would be advantageous to that of qubit based simulation of the Abelian Higgs and other SU(3) based gauge theories, and various spin-1 models.

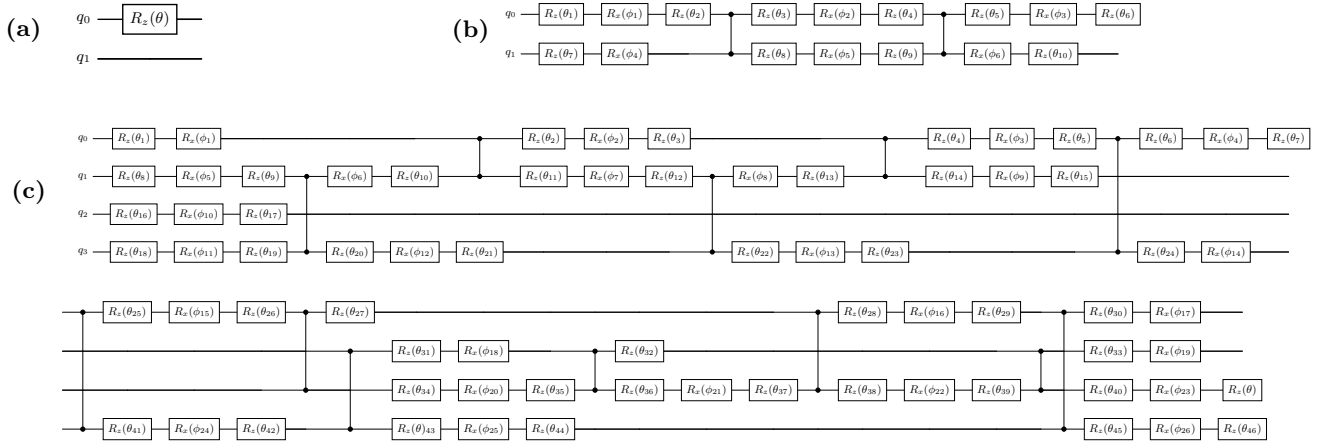


FIG. 13: Transpiler-compiled qubit-gate decomposition of the different operations in the Trotterized evolution of the spin-1 truncated AHM. With binary encoding, decomposition of the (a) M_z , (b) M_x , and (c) M_{zz} operations are shown. Numerical rotation angles of different operations are replaced with symbols for visual clarity. Note the increase in the number of entangling operations for the qubit decomposition compared to the qutrit decomposition and the presence of non-local entangling operations in the qubit formulation. In the absence of all-to-all connectivity of the qubits, the number of entangling operation increases further due to the presence of additional swap gates between qubit pairs. Each SWAP operation introduces three entangling gates, thus rendering the qubit decomposition even more costly.

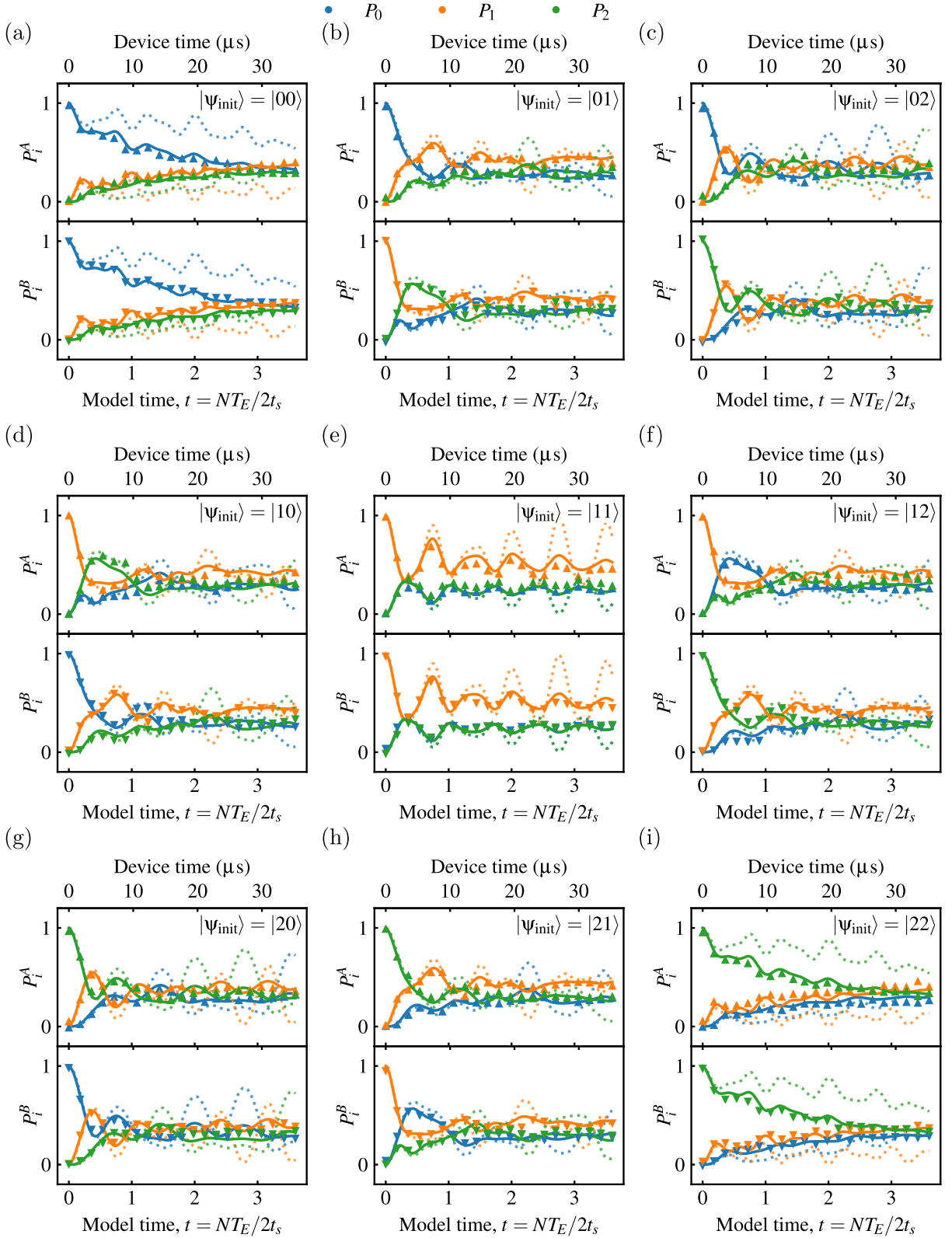


FIG. 14: Two-qutrit analog-digital experimental results, extended. Data shown in Fig. 4(b) is excerpted from (h). Dotted lines show exact evolution of the AHM under the Schrödinger equation, solid lines show evolution under the Lindblad model described in Appendix F, and triangle markers are experimentally measured transmon eigenstate probabilities, after a statistical readout correction has been applied. Model parameters were $\kappa/2\pi = \chi/2\pi = \beta/2\pi = 1$, and the scale frequency for all measurements was $t_s^{-1} \approx 110$ kHz. Uncertainties are estimated from shot noise $\sigma \sim 1/\sqrt{N_{\text{shots}}}$ where $N_{\text{shots}} = 3000$. Error bars are smaller than the markers.

- [1] M. Troyer and U.-J. Wiese, Computational complexity and fundamental limitations to fermionic quantum Monte Carlo simulations, *Phys. Rev. Lett.* **94**, 170201 (2005), [arXiv:cond-mat/0408370](#).
- [2] C. Gatteringer and K. Langfeld, Approaches to the sign problem in lattice field theory, *Int. J. Mod. Phys. A* **31**, 1643007 (2016), [arXiv:1603.09517 \[hep-lat\]](#).
- [3] E. Zohar, Quantum simulation of lattice gauge theories in more than one space dimension—requirements, challenges and methods, *Phil. Trans. A. Math. Phys. Eng. Sci.* **380**, 20210069 (2021), [arXiv:2106.04609 \[quant-ph\]](#).
- [4] C. Charles, E. J. Gustafson, E. Hardt, F. Herren, N. Hogan, H. Lamm, S. Starecheski, R. S. Van de Water, and M. L. Wagman, Simulating Z2 lattice gauge theory on a quantum computer, *Phys. Rev. E* **109**, 015307 (2024), [arXiv:2305.02361 \[hep-lat\]](#).
- [5] A. Bazavov, Y. Meurice, S.-W. Tsai, J. Unmuth-Yockey, and J. Zhang, Gauge-invariant implementation of the Abelian Higgs model on optical lattices, *Phys. Rev. D* **92**, 076003 (2015), [arXiv:1503.08354 \[hep-lat\]](#).
- [6] E. A. Martinez *et al.*, Real-time dynamics of lattice gauge theories with a few-qubit quantum computer, *Nature* **534**, 516 (2016), [arXiv:1605.04570 \[quant-ph\]](#).
- [7] A. De *et al.*, Observation of string-breaking dynamics in a quantum simulator, (2024), [arXiv:2410.13815 \[quant-ph\]](#).
- [8] D. Luo *et al.*, Quantum simulation of bubble nucleation across a quantum phase transition, (2025), [arXiv:2505.09607 \[quant-ph\]](#).
- [9] R. G. Jha, A. Milsted, D. Neuenfeld, J. Preskill, and P. Vieira, Real-time scattering in Ising field theory using matrix product states, *Phys. Rev. Res.* **7**, 023266 (2025), [arXiv:2411.13645 \[hep-th\]](#).
- [10] H. Lamm, S. Lawrence, and Y. Yamauchi, General Methods for Digital Quantum Simulation of Gauge Theories, *Phys. Rev. D* **100**, 034518 (2019), [arXiv:1903.08807 \[hep-lat\]](#).
- [11] D. Gonzalez-Cuadra *et al.*, Observation of string breaking on a (2 + 1)D Rydberg quantum simulator, *Nature* **642**, 321 (2025), [arXiv:2410.16558 \[quant-ph\]](#).
- [12] A. Yamamoto, Real-time simulation of (2+1)-dimensional lattice gauge theory on qubits, *PTEP* **2021**, 013B06 (2021), [arXiv:2008.11395 \[hep-lat\]](#).
- [13] Y. Ding, X. Cui, and Y. Shi, Digital quantum simulation and pseudoquantum simulation of the Z2 gauge-Higgs model, *Phys. Rev. D* **105**, 054508 (2022), [arXiv:2108.13410 \[hep-lat\]](#).
- [14] S. Maiti, D. Banerjee, B. Chakraborty, and E. Huffman, Spontaneous symmetry breaking in a SO(3) non-Abelian lattice gauge theory in 2+1D with quantum algorithms, *Phys. Rev. Res.* **7**, 013283 (2025), [arXiv:2409.07108 \[hep-lat\]](#).
- [15] N. Mueller, T. Wang, O. Katz, Z. Davoudi, and M. Cetina, Quantum computing universal thermalization dynamics in a (2+1)D Lattice Gauge Theory, *Nature Commun.* **16**, 5492 (2025), [arXiv:2408.00069 \[quant-ph\]](#).
- [16] H. Sukeno and T. Okuda, Measurement-based quantum simulation of Abelian lattice gauge theories, *SciPost Phys.* **14**, 129 (2023), [arXiv:2210.10908 \[quant-ph\]](#).
- [17] L. Homeier, A. Bohrdt, S. Linsel, E. Demler, J. C. Halimeh, and F. Grusdt, Realistic scheme for quantum simulation of \mathbb{Z}_2 lattice gauge theories with dynamical matter in (2 + 1)D, *Commun. Phys.* **6**, 127 (2023), [arXiv:2205.08541 \[cond-mat.quant-gas\]](#).
- [18] M. Meth, J. Zhang, J. F. Haase, C. Edmunds, L. Postler, A. J. Jena, A. Steiner, L. Dellantonio, R. Blatt, P. Zoller, T. Monz, P. Schindler, C. Muschik, and M. Ringbauer, Simulating two-dimensional lattice gauge theories on a qudit quantum computer, *Nature Physics* **21**, 570 (2025), publisher: Nature Publishing Group.
- [19] T. A. Cochran *et al.*, Visualizing dynamics of charges and strings in (2 + 1)D lattice gauge theories, *Nature* **642**, 315 (2025).
- [20] E. O. Rosanowski, A. Crippa, L. Funcke, P. V. Itaborai, K. Jansen, and S. Singh, (2+1)D Quantum Electrodynamics at Finite Density on a Quantum Computer, (2025), [arXiv:2509.20558 \[hep-lat\]](#).
- [21] D.-S. Xiang *et al.*, Real-time scattering and freeze-out dynamics in Rydberg-atom lattice gauge theory, (2025), [arXiv:2508.06639 \[cond-mat.quant-gas\]](#).
- [22] Z.-Y. Zhou, G.-X. Su, J. C. Halimeh, R. Ott, H. Sun, P. Hauke, B. Yang, Z.-S. Yuan, J. Berges, and J.-W. Pan, Thermalization dynamics of a gauge theory on a quantum simulator, *Science* **377**, ab16277 (2022), [arXiv:2107.13563 \[cond-mat.quant-gas\]](#).
- [23] J. Jiang, N. Kleo, and O. Di Matteo, Non-Abelian dynamics on a cube: Improving quantum compilation through qudit-based simulations, *Phys. Rev. D* **112**, 074512 (2025), [arXiv:2506.10945 \[quant-ph\]](#).
- [24] D. M. Kurcuoglu, M. S. Alam, J. A. Job, A. C. Y. Li, A. Macridin, G. N. Perdue, and S. Providence, Quantum simulation of ϕ^4 theories in qudit systems, (2021), [arXiv:2108.13357 \[quant-ph\]](#).
- [25] E. Gustafson, *Noise Improvements in Quantum Simulations of sQED using Qutrits* (2022), [arXiv:2201.04546 \[hep-lat, physics.quant-ph\]](#).
- [26] M. Illa, C. E. P. Robin, and M. J. Savage, Qu8its for quantum simulations of lattice quantum chromodynamics, *Physical Review D* **110**, 014507 (2024), publisher: American Physical Society.
- [27] M. S. Blok, V. V. Ramasesh, T. Schuster, K. O'Brien, J. M. Kreikebaum, D. Dahlen, A. Morvan, B. Yoshida, N. Y. Yao, and I. Siddiqi, Quantum Information Scrambling on a Superconducting Qutrit Processor, *Phys. Rev. X* **11**, 021010 (2021), [arXiv:2003.03307 \[quant-ph\]](#).
- [28] T. Roy, Z. Li, E. Kapit, and D. Schuster, Two-Qutrit Quantum Algorithms on a Programmable Superconducting Processor, *Physical Review Applied* **19**, 064024 (2023).
- [29] M. Ringbauer, M. Meth, L. Postler, R. Stricker, R. Blatt, P. Schindler, and T. Monz, A universal qudit quantum processor with trapped ions, *Nature Physics* **18**, 1053 (2022), number: 9 Publisher: Nature Publishing Group.
- [30] Y. Chi, J. Huang, Z. Zhang, J. Mao, Z. Zhou, X. Chen, C. Zhai, J. Bao, T. Dai, H. Yuan, M. Zhang, D. Dai, B. Tang, Y. Yang, Z. Li, Y. Ding, L. K. Oxenløwe, M. G. Thompson, J. L. O'Brien, Y. Li, Q. Gong, and J. Wang, A programmable qudit-based quantum processor, *Nature Communications* **13**, 1166 (2022), publisher: Nature Publishing Group.

- [31] A. Ciavarella, N. Klco, and M. J. Savage, Trailhead for quantum simulation of SU(3) Yang-Mills lattice gauge theory in the local multiplet basis, *Phys. Rev. D* **103**, 094501 (2021), arXiv:2101.10227 [quant-ph].
- [32] E. J. Gustafson, Prospects for simulating a qudit-based model of (1 + 1) D scalar QED, *Physical Review D* **103**, 114505 (2021).
- [33] Y. Meurice, Theoretical methods to design and test quantum simulators for the compact Abelian Higgs model, *Phys. Rev. D* **104**, 094513 (2021), arXiv:2107.11366 [quant-ph].
- [34] D. González-Cuadra, T. V. Zache, J. Carrasco, B. Kraus, and P. Zoller, Hardware Efficient Quantum Simulation of Non-Abelian Gauge Theories with Qudits on Rydberg Platforms, *Physical Review Letters* **129**, 160501 (2022), publisher: American Physical Society.
- [35] T. V. Zache, D. González-Cuadra, and P. Zoller, Fermion-qudit quantum processors for simulating lattice gauge theories with matter, *Quantum* **7**, 1140 (2023), publisher: Verein zur Förderung des Open Access Publizierens in den Quantenwissenschaften.
- [36] M. Ila, C. E. P. Robin, and M. J. Savage, Quantum simulations of SO(5) many-fermion systems using qudits, *Physical Review C* **108**, 064306 (2023), publisher: American Physical Society.
- [37] P. P. Popov, M. Meth, M. Lewenstein, P. Hauke, M. Ringbauer, E. Zohar, and V. Kasper, Variational quantum simulation of U(1) lattice gauge theories with qudit systems, *Phys. Rev. Res.* **6**, 013202 (2024).
- [38] G. Calajó, G. Magnifico, C. Edmunds, M. Ringbauer, S. Montangero, and P. Silvi, Digital Quantum Simulation of a (1+1)D SU(2) Lattice Gauge Theory with Ion Qudits, *PRX Quantum* **5**, 040309 (2024).
- [39] G. Calliari, M. Di Liberto, H. Pichler, and T. V. Zache, Quantum Simulating Continuum Field Theories with Large-Spin Lattice Models, *PRX Quantum* **6**, 030304 (2025).
- [40] J. Jiang, N. Klco, and O. Di Matteo, Non-Abelian dynamics on a cube: Improving quantum compilation through qudit-based simulations, *Phys. Rev. D* **112**, 074512 (2025).
- [41] M. E. Peskin and D. V. Schroeder, *An Introduction to quantum field theory* (Addison-Wesley, Reading, USA, 1995).
- [42] E. H. Fradkin and S. H. Shenker, Phase Diagrams of Lattice Gauge Theories with Higgs Fields, *Phys. Rev. D* **19**, 3682 (1979).
- [43] M. B. Einhorn and R. Savit, Phase Transitions in the Abelian Higgs Model, *Phys. Rev. D* **19**, 1198 (1979).
- [44] D. J. Callaway and L. J. Carson, Abelian higgs model: A monte carlo study, *Physical Review D* **25**, 531 (1982).
- [45] A. M. Polyakov, Quark confinement and topology of gauge theories, *Nuclear Physics B* **120**, 429 (1977).
- [46] F. A. Schaposnik, Pseudoparticles and Confinement in the Two-Dimensional Abelian Higgs Model, *Phys. Rev. D* **18**, 1183 (1978).
- [47] J. Koch, T. M. Yu, J. Gambetta, A. A. Houck, D. I. Schuster, J. Majer, A. Blais, M. H. Devoret, S. M. Girvin, and R. J. Schoelkopf, Charge-insensitive qubit design derived from the Cooper pair box, *Phys. Rev. A* **76**, 042319 (2007), arXiv:cond-mat/0703002.
- [48] R. Bianchetti, S. Filipp, M. Baur, J. M. Fink, C. Lang, L. Steffen, M. Boissonneault, A. Blais, and A. Wallraff, Control and Tomography of a Three Level Superconducting Artificial Atom, *Physical Review Letters* **105**, 223601 (2010).
- [49] Y. Cho, K. M. Beck, A. R. Castelli, K. A. Wendt, B. Evert, M. J. Reagor, and J. L. DuBois, Direct pulse-level compilation of arbitrary quantum logic gates on superconducting qutrits, *Physical Review Applied* **22**, 034066 (2024).
- [50] K. Kumaran, F. Alam, N. Eassa, K. Ferris, X. Xiao, L. Cincio, N. Bronn, and A. Banerjee, *Transmon qutrit-based simulation of spin-1 AKLT systems* (2025), arXiv:2412.19786 [quant-ph].
- [51] N. Ticea, E. Portoles, E. Rosenberg, A. Schuckert, A. Szasz, B. Kobrin, N. Pomata, P. Praneel, C. Miao, S. Kumar, *et al.*, *Observation of disorder-induced superfluidity* (2026), arXiv:2512.21416 [quant-ph].
- [52] D. Hayes, S. T. Flammia, and M. J. Biercuk, Programmable quantum simulation by dynamic Hamiltonian engineering, *New Journal of Physics* **16**, 083027 (2014), publisher: IOP Publishing.
- [53] I. Arrazola, J. S. Pedernales, L. Lamata, and E. Solano, Digital-Analog Quantum Simulation of Spin Models in Trapped Ions, *Scientific Reports* **6**, 30534 (2016), publisher: Nature Publishing Group.
- [54] S. Choi, N. Y. Yao, and M. D. Lukin, Dynamical Engineering of Interactions in Qudit Ensembles, *Physical Review Letters* **119**, 183603 (2017), publisher: American Physical Society.
- [55] N. K. Langford, R. Sagastizabal, M. Kounalakis, C. Dickel, A. Bruno, F. Luthi, D. J. Thoen, A. Endo, and L. DiCarlo, Experimentally simulating the dynamics of quantum light and matter at deep-strong coupling, *Nature Communications* **8**, 1715 (2017), publisher: Nature Publishing Group.
- [56] D. V. Babukhin, A. A. Zhukov, and W. V. Pogosov, Hybrid digital-analog simulation of many-body dynamics with superconducting qubits, *Physical Review A* **101**, 052337 (2020), publisher: American Physical Society.
- [57] T. I. t. Andersen, Thermalization and criticality on an analogue-digital quantum simulator, *Nature* **638**, 79 (2025), publisher: Nature Publishing Group.
- [58] J. Choi, H. Zhou, H. S. Knowles, R. Landig, S. Choi, and M. D. Lukin, Robust dynamic hamiltonian engineering of many-body spin systems, *Phys. Rev. X* **10**, 031002 (2020).
- [59] H. Zhou, H. Gao, N. T. Leitaó, O. Makarova, I. Cong, A. M. Douglas, L. S. Martin, and M. D. Lukin, Robust hamiltonian engineering for interacting qudit systems, *Phys. Rev. X* **14**, 031017 (2024).
- [60] W. Morong, K. Collins, A. De, E. Stavropoulos, T. You, and C. Monroe, Engineering Dynamically Decoupled Quantum Simulations with Trapped Ions, *PRX Quantum* **4**, 010334 (2023), publisher: American Physical Society.
- [61] P. Scholl, H. J. Williams, G. Bornet, F. Wallner, D. Barredo, L. Henriot, A. Signoles, C. Hainaut, T. Franz, S. Geier, A. Tebben, A. Salzinger, G. Zürn, T. Lahaye, M. Weidemüller, and A. Browaeys, Microwave Engineering of Programmable $\$XXZ\$$ Hamiltonians in Arrays of Rydberg Atoms, *PRX Quantum* **3**, 020303 (2022), publisher: American Physical Society.
- [62] A. Morvan, V. V. Ramasesh, M. S. Blok, J. M. Kreikebaum, K. O'Brien, L. Chen, B. K. Mitchell, R. K. Naik, D. I. Santiago, and I. Siddiqi, Qutrit Randomized Benchmarking, *Phys. Rev. Lett.* **126**, 210504 (2021),

- arXiv:2008.09134 [quant-ph].
- [63] N. Goss, S. Ferracin, A. Hashim, A. Carignan-Dugas, J. M. Kreikebaum, R. K. Naik, D. I. Santiago, and I. Siddiqi, Extending the computational reach of a superconducting qutrit processor, *npj Quantum Inf.* **10**, 101 (2024), arXiv:2305.16507 [quant-ph].
- [64] M. B. Einhorn and R. Savit, Phase transitions and confinement in the abelian higgs model, *Physical Review D* **19**, 1198 (1979).
- [65] T. Banks and E. Rabinovici, Finite Temperature Behavior of the Lattice Abelian Higgs Model, *Nucl. Phys. B* **160**, 349 (1979).
- [66] A. M. Polyakov, *Gauge fields and strings* (Routledge, 2018).
- [67] J. C. Halimeh, N. Mueller, J. Knolle, Z. Papić, and Z. Davoudi, Quantum simulation of out-of-equilibrium dynamics in gauge theories, (2025), arXiv:2509.03586 [quant-ph].
- [68] J. Li, G. S. Paraoanu, K. Cicak, F. Altomare, J. I. Park, R. W. Simmonds, M. A. Sillanpää, and P. J. Hakonen, Decoherence, Autler-Townes effect, and dark states in two-tone driving of a three-level superconducting system, *Physical Review B* **84**, 104527 (2011).
- [69] P. Krantz, M. Kjaergaard, F. Yan, T. P. Orlando, S. Gustavsson, and W. D. Oliver, A quantum engineer's guide to superconducting qubits, *Applied Physics Reviews* **6**, 021318 (2019).
- [70] A. Brinkmann, Introduction to average hamiltonian theory. i. basics, *Concepts in Magnetic Resonance Part A* **45**, e21414 (2016).
- [71] S. Bravyi, S. Sheldon, A. Kandala, D. C. McKay, and J. M. Gambetta, Mitigating measurement errors in multiqubit experiments, *Physical Review A* **103**, 042605 (2021), publisher: American Physical Society.
- [72] Z. Wang, R. W. Parker, E. Champion, and M. S. Blok, High- E_J/E_C transmon qudits with up to 12 levels, *Physical Review Applied* **23**, 034046 (2025), publisher: American Physical Society.
- [73] M. Elliott, J. Joo, and E. Ginossar, Designing Kerr interactions using multiple superconducting qubit types in a single circuit, *New J. Phys.* **20**, 023037 (2018).
- [74] M. Malekakhlagh, E. Magesan, and D. C. McKay, First-principles analysis of cross-resonance gate operation, *Physical Review A* **102**, 042605 (2020), publisher: American Physical Society.
- [75] J. R. Garbow, D. P. Weitekamp, and A. Pines, Bilinear rotation decoupling of homonuclear scalar interactions, *Chemical Physics Letters* **93**, 504 (1982).
- [76] M. Takita, A. W. Cross, A. D. Córcoles, J. M. Chow, and J. M. Gambetta, Experimental Demonstration of Fault-Tolerant State Preparation with Superconducting Qubits, *Physical Review Letters* **119**, 180501 (2017), publisher: American Physical Society.
- [77] L. M. K. Vandersypen and I. L. Chuang, NMR techniques for quantum control and computation, *Reviews of Modern Physics* **76**, 1037 (2005), publisher: American Physical Society.
- [78] N. Goss, A. Morvan, B. Marinelli, B. K. Mitchell, L. B. Nguyen, R. K. Naik, L. Chen, C. Jünger, J. M. Kreikebaum, D. I. Santiago, J. J. Wallman, and I. Siddiqi, High-fidelity qutrit entangling gates for superconducting circuits, *Nature Communications* **13**, 7481 (2022).
- [79] A. M. Forney, S. R. Jackson, and F. W. Strauch, Multi-frequency control pulses for multilevel superconducting quantum circuits, *Physical Review A* **81**, 012306 (2010), publisher: American Physical Society.
- [80] E. Champion, Z. Wang, R. Parker, and M. Blok, Multi-frequency control and measurement of a spin-7/2 system encoded in a transmon qudit (2024), arXiv:2405.15857 [quant-ph].
- [81] N. Lambert, E. Giguère, P. Menczel, B. Li, P. Hopf, G. Suárez, M. Gali, J. Lishman, R. Gadhvi, R. Agarwal, A. Galicia, N. Shammah, P. Nation, J. R. Johansson, S. Ahmed, S. Cross, A. Pitchford, and F. Nori, Qutip 5: The quantum toolbox in python, (2024), arXiv:2412.04705 [quant-ph].
- [82] D. C. McKay, C. J. Wood, S. Sheldon, J. M. Chow, and J. M. Gambetta, Efficient Z gates for quantum computing, *Physical Review A* **96**, 022330 (2017), publisher: American Physical Society.
- [83] D. Gottesman, Fault-Tolerant Quantum Computation with Higher-Dimensional Systems, *Chaos, Solitons & Fractals* **10**, 1749 (1999).
- [84] Y.-M. Di and H.-R. Wei, Synthesis of multivalued quantum logic circuits by elementary gates, *Phys. Rev. A* **87**, 012325 (2013).
- [85] S. J. Beale, A. Carignan-Dugas, D. Dahlen, J. Emerson, I. Hincks, P. Iyer, A. Jain, D. Hufnagel, E. Ospadov, J. Saunders, *et al.*, True-q, Version **2**, 13 (2020).
- [86] $SU(3)$ appears as the color gauge group of QCD and in the low energy limit applying massless quark approximation we get an effective low energy theory that has global left-right symmetry $SU(3)_L \times SU(3)_R$ which is spontaneously broken to $SU(3)$ vector symmetry due to chiral condensate.
- [87] E. Magesan, J. M. Gambetta, and J. Emerson, Scalable and Robust Randomized Benchmarking of Quantum Processes, *Phys. Rev. Lett.* **106**, 180504 (2011), arXiv:1009.3639 [quant-ph].
- [88] E. Magesan *et al.*, Efficient Measurement of Quantum Gate Error by Interleaved Randomized Benchmarking, *Phys. Rev. Lett.* **109**, 080505 (2012), arXiv:1203.4550 [quant-ph].
- [89] A. Hashim, R. K. Naik, A. Morvan, J.-L. Ville, B. Mitchell, J. M. Kreikebaum, M. Davis, E. Smith, C. Iancu, K. P. O'Brien, I. Hincks, J. J. Wallman, J. Emerson, and I. Siddiqi, Randomized compiling for scalable quantum computing on a noisy superconducting quantum processor, *Phys. Rev. X* **11**, 041039 (2021).
- [90] A. Erhard, J. J. Wallman, L. Postler, M. Meth, R. Stricker, E. A. Martinez, P. Schindler, T. Monz, J. Emerson, and R. Blatt, Characterizing large-scale quantum computers via cycle benchmarking, *Nature Commun.* **10**, 5347 (2019), arXiv:1902.08543 [quant-ph].
- [91] A. Carignan-Dugas, D. Dahlen, I. Hincks, E. Ospadov, S. J. Beale, S. Ferracin, J. Skanes-Norman, J. Emerson, and J. J. Wallman, The Error Reconstruction and Compiled Calibration of Quantum Computing Cycles, (2023), arXiv:2303.17714 [quant-ph].
- [92] *Cirq* (Zenodo, 2025).
- [93] J. Wilkens, M. Ioannou, E. Derbyshire, J. Eisert, D. Hangleiter, I. Roth, and J. Haferkamp, Benchmarking bosonic and fermionic dynamics (2024), arXiv:2408.11105 [quant-ph].
- [94] V. P. Canelles, M. G. Algaba, H. Heimonen, M. Papić, M. Ponce, J. Rönkkö, M. J. Thapa, I. d. Vega, and A. Auer, Benchmarking Digital-Analog Quantum Com-

- putation (2023), arXiv:2307.07335 [quant-ph].
- [95] C. H. Valahu, T. Navickas, M. J. Biercuk, and T. R. Tan, Benchmarking Bosonic Modes for Quantum Information with Randomized Displacements, *PRX Quantum* **5**, 040337 (2024), publisher: American Physical Society.
- [96] T. Steckmann, D. Luo, Y.-X. Wang, S. R. Muleady, A. Seif, C. Monroe, M. J. Gullans, A. V. Gorshkov, O. Katz, and A. Schuckert, Error mitigation of shot-to-shot fluctuations in analog quantum simulators (2025), arXiv:2506.16509 [quant-ph].
- [97] R.-C. Guo, Y. Gu, and D. E. Liu, Mitigating errors in analog quantum simulation by Hamiltonian reshaping or Hamiltonian rescaling, *npj Quantum Information* **11**, 14 (2025), publisher: Nature Publishing Group.
- [98] N. A. Zemlevskiy, H. F. Froland, and S. Caspar, Optimization of algorithmic errors in analog quantum simulations, *Physical Review A* **109**, 052425 (2024), publisher: American Physical Society.
- [99] F. Petiziol, M. Sameti, S. Carretta, S. Wimberger, and F. Mintert, Quantum Simulation of Three-Body Interactions in Weakly Driven Quantum Systems, *Phys. Rev. Lett.* **126**, 250504 (2021).
- [100] L. B. Nguyen, N. Goss, K. Siva, Y. Kim, E. Younis, B. Qing, A. Hashim, D. I. Santiago, and I. Siddiqi, Empowering a qudit-based quantum processor by traversing the dual bosonic ladder, *Nat Commun* **15**, 7117 (2024).
- [101] E. Champion, A. Schwartz, M. A. Ijaz, X. Xu, S. Campbell, G. T. Landi, and M. S. Blok, Analog quantum simulation of the Lipkin-Meshkov-Glick model in a transmon qudit (2025), version Number: 1.
- [102] U. Haebleren and J. S. Waugh, Coherent Averaging Effects in Magnetic Resonance, *Phys. Rev.* **175**, 453 (1968).
- [103] W. Magnus, On the exponential solution of differential equations for a linear operator, *Commun. Pure Appl. Math.* **7**, 649 (1954).
- [104] S. Blanes, F. Casas, J. A. Oteo, and J. Ros, The Magnus expansion and some of its applications, *Phys. Rep.* **470**, 151 (2009).
- [105] J. M. Gambetta, F. Motzoi, S. T. Merkel, and F. K. Wilhelm, Analytic control methods for high-fidelity unitary operations in a weakly nonlinear oscillator, *Physical Review A* **83**, 012308 (2011), publisher: American Physical Society.
- [106] B. Li, F. Cárdenas-López, A. Lupascu, and F. Motzoi, Universal Pulses for Superconducting Qudit Ladder Gates, *PRX Quantum* **6**, 030357 (2025), publisher: American Physical Society.
- [107] P. Groszkowski and J. Koch, Scqubits: a Python package for superconducting qubits, *Quantum* **5**, 583 (2021).
- [108] S. P. Chitta, T. Zhao, Z. Huang, I. Mondragon-Shem, and J. Koch, Computer-aided quantization and numerical analysis of superconducting circuits, *New J. Phys.* **24**, 103020 (2022).
- [109] A. Messiah, *Quantum Mechanics*, 1st ed., Vol. 2 (John Wiley & Sons, Inc., New York, 1962).
- [110] B. K. Mitchell, R. K. Naik, A. Morvan, A. Hashim, J. M. Kreikebaum, B. Marinelli, W. Lavrijsen, K. Nowrouzi, D. I. Santiago, and I. Siddiqi, Hardware-Efficient Microwave-Activated Tunable Coupling between Superconducting Qubits, *Physical Review Letters* **127**, 200502 (2021), publisher: American Physical Society.
- [111] K. X. Wei, E. Magesan, I. Lauer, S. Srinivasan, D. F. Bogorin, S. Carnevale, G. A. Keefe, Y. Kim, D. Klaus, W. Landers, N. Sundaresan, C. Wang, E. J. Zhang, M. Steffen, O. E. Dial, D. C. McKay, and A. Kandala, Hamiltonian Engineering with Multicolor Drives for Fast Entangling Gates and Quantum Crosstalk Cancellation, *Physical Review Letters* **129**, 060501 (2022), publisher: American Physical Society.
- [112] C. Cohen-Tannoudji, J. Dupont-Roc, and G. Grynberg, *Atom-photon Interactions: Basic Processes and Applications*, Physics textbook (Wiley, Weinheim-VCH, 2004).
- [113] Y. Y. Gao, M. A. Rol, S. Touzard, and C. Wang, Practical Guide for Building Superconducting Quantum Devices, *PRX Quantum* **2**, 040202 (2021), publisher: American Physical Society.
- [114] J. Schwinger, Unitary operator bases, *Proceedings of the National Academy of Sciences* **46**, 570 (1960), publisher: Proceedings of the National Academy of Sciences.
- [115] H. Carmichael, *An Open Systems Approach to Quantum Optics: Lectures Presented at the Université Libre de Bruxelles October 28 to November 4, 1991*, edited by H. Araki, E. Brézin, J. Ehlers, U. Frisch, K. Hepp, R. L. Jaffe, R. Kippenhahn, H. A. Weidenmüller, J. Wess, J. Zittartz, and W. Beiglböck, Lecture Notes in Physics Monographs, Vol. 18 (Springer Berlin Heidelberg, Berlin, Heidelberg, 1993).
- [116] J. Li, M. A. Sillanpää, G. S. Paraoanu, and P. J. Hakonen, Pure dephasing in a superconducting three-level system, *J. Phys.: Conf. Ser.* **400**, 042039 (2012).
- [117] H.-P. Breuer and F. Petruccione, *The theory of open quantum systems* (OUP Oxford, 2002).
- [118] F. Turro, T. Chistolini, A. Hashim, Y. Kim, W. Livingston, J. M. Kreikebaum, K. A. Wendt, J. L. Dubois, F. Pederiva, S. Quaglioni, D. I. Santiago, and I. Siddiqi, Demonstration of a quantum-classical coprocessing protocol for simulating nuclear reactions, *Phys. Rev. A* **108**, 032417 (2023).
- [119] M. A. Graydon, J. Skanes-Norman, and J. J. Wallman, Designing Stochastic Channels, (2022), arXiv:2201.07156 [quant-ph].
- [120] A. Hashim *et al.*, Practical Introduction to Benchmarking and Characterization of Quantum Computers, *PRX Quantum* **6**, 030202 (2025), arXiv:2408.12064 [quant-ph].
- [121] N. P. D. Sawaya, T. Menke, T. H. Kyaw, S. Johri, A. Aspuru-Guzik, and G. G. Guerreschi, Resource-efficient digital quantum simulation of d-level systems for photonic, vibrational, and spin-s Hamiltonians, *npj Quantum Inf.* **6**, 49 (2020), arXiv:1909.12847 [quant-ph].
- [122] E. Younis, C. C. Iancu, W. Lavrijsen, M. Davis, and E. Smith, Berkeley quantum synthesis toolkit (bqskit) v1, [Computer Software] <https://doi.org/10.11578/dc.20210603.2> (2021).